Distinct Colitis-Associated Macrophages Drive NOD2-Dependent Bacterial Sensing and Gut Homeostasis

Authors: Gajanan D. Katkar[1†], Mahitha Shree Anandachar[1,2†], Stella-Rita Ibeawuchi[2], Celia R. Espinoza[1], Jane Coates[1], Yashaswat S. Malhotra[1], Madhubanti Mullick[1], Vanessa Castillo[1], Daniella T. Vo[3], Debashis Sahoo[4], Saptarshi Sinha[1], and Pradipta Ghosh[1,5*]

Affiliations:
[1]Department of Cellular and Molecular Medicine, University of California San Diego, CA, USA.
[2]Department of Pathology, University of California San Diego, CA, USA.
[3]Department of Pediatrics, University of California San Diego, CA, USA.
[4]Department of Computer Science and Engineering, University of California San Diego, CA, USA.
[5]Department of Medicine, University of California San Diego, CA, USA.

[†] Equal contribution

Conflict of interest statement: Authors have declared that no conflict of interest exists.

KEY WORDS: GIV/Girdin, Guanine-nucleotide exchange modulators (GEMs), CCDC88A, Macrophage, NOD2, MDP, Microbes, Innate immunity

***Correspondence to**:

Pradipta Ghosh, M.D.; Professor, Departments of Medicine, and Cell and Molecular Medicine, University of California San Diego; 9500 Gilman Drive (MC 0651), George E. Palade Bldg, Rm 232, 239; La Jolla, CA 92093. Phone: 858-822-7633: Fax: 858-822-7636: Email: prghosh@ucsd.edu

ABSTRACT (218-words)

Single-cell studies have revealed that intestinal macrophages maintain gut homeostasis through the balanced actions of reactive (inflammatory "accelerators") and tolerant (non-inflammatory "brakes") subpopulations. How these populations function in inflammatory bowel diseases (IBD), including Crohn's disease (CD) and ulcerative colitis (UC), remains unresolved. Using multi-omics data and computational tools, here we define colon-specific macrophage states and reveal the critical role of non-inflammatory colon-associated macrophages (ni-ColAMs) in IBD recovery. Through trans-scale analyses—integrating computational transcriptomics, proteomics, and *in vivo* interventional studies—we pinpointed GIV (*CCDC88A*), a heterotrimeric G-protein modulator, as a key regulator of ni-ColAMs. Notably, GIV emerged as the top-ranked gene in ni-ColAMs that physically and functionally interacts with nucleotide-binding oligomerization domain-containing protein 2 (NOD2), an innate immune sensor implicated in both CD and UC. Myeloid-specific depletion of GIV exacerbates infectious colitis, prolongs disease course, and abolishes the protective effects of muramyl dipeptide (MDP) in chemical colitis and sepsis models. GIV is required for NOD2 to dampen inflammation and efficiently clear microbes. GIV binds directly to NOD2's terminal leucine-rich repeat (LRR#10) via its C-terminus. This interaction is disrupted in the CD-associated *1007fs* NOD2 variant, which lacks LRR#10, leading to impaired bacterial sensing and clearance. Findings illuminate how GIV and NOD2 collaborate to maintain gut homeostasis and reveal how derailment of such collaboration may drive dysbiosis and inflammation in IBD.

INTRODUCTION

Intestinal macrophages are critical for gut development, immunity and repair (1). Single-cell studies have revealed that gut homeostasis relies on the dynamic interplay between two antagonistic macrophage subpopulations: inflammatory "accelerators" and non-inflammatory "brakes" (2, 3). An imbalance in these subpopulations can lead to uncontrolled gut inflammation, as observed in inflammatory bowel diseases (IBD) such as Crohn's disease (CD) and ulcerative colitis (UC) (4, 5). However, precisely defining these subpopulations and understanding their roles in health and disease, and molecular mechanisms that control the same remain significant challenges (6).

Recent advances in artificial intelligence (AI) and machine learning-guided transcriptomics have addressed this challenge by enabling the analysis of diverse macrophage states across bulk and single-cell datasets (3, 7-10). Among these approaches, Boolean implication networks have emerged as a robust method with a decade-long track record (7, 8, 11, 12) for identifying universally conserved gene expression patterns (or "invariants"). These patterns remain consistent despite the variability introduced by tissue heterogeneity, circadian rhythms, metabolic states, species diversity, perturbations, stimuli, and disease conditions (7, 8, 11, 12).

Here we used human tissue transcriptomes and gene signatures derived from Boolean implication networks; we formally defined two macrophage subpopulations in the colon: inflammatory (i-ColAMs) and non-inflammatory (ni-ColAMs)---both in health and IBD. Our findings reveal that tolerant ni-ColAMs are essential for dampening inflammation and resolving infections, making them critical for recovery from IBD. Notably, we identified a previously unappreciated yet consequential physical and functional coupling in IBD-associated ni-ColAMs between the innate immune sensor nucleotide-binding oligomerization domain-containing protein 2 (NOD2) and GIV (Gα-interacting vesicle-associated protein, also known as Girdin). GIV, a multi-modular signaling scaffold and heterotrimeric G protein modulator, interacts dynamically with NOD2 to facilitate microbial sensing and clearance while suppressing inflammation. This protective mechanism, unique to ni-ColAMs, is disrupted in the most clinically significant IBD-associated NOD2 risk variant, underscoring its relevance to disease pathology. These insights shed new light on the molecular pathways underlying gut homeostasis and the progression of IBD, offering potential therapeutic avenues for restoring balance in macrophage subpopulations.

RESULTS

Identification of distinct subpopulations of colon-associated macrophages

Using Boolean implication network approach, we recently identified 338 conserved genes within a model of macrophage continuum states, which we called '*S*ignature of *Ma*crophage *R*eactivity and *T*olerance' (SMaRT; see **Fig 1A,** Supplemental information 1) (3). Of the 338 genes, high expression of 48 genes and low expression of 290 genes defines reactive macrophages, whereas the opposite pattern (low-48, high-290) defines tolerant macrophages (3). The SMaRT model provides a computational framework for tracking invariant patterns in gene expression that accompany dynamic shifts in macrophage function across the physiologic and pathologic spectra of "reactivity" and "tolerance" regardless of species or tissue type and agnostic of disease state(s) (3). To contextualize the SMaRT model in the setting of the human gut, and

specifically to IBD, we refined the model by training it on the largest, high quality, full-thickness colon tissue transcriptomic dataset of IBD (GSE83687) (13); the only one of its kind on NCBI GEO). Briefly, we employed machine learning based classifier on 338 SMaRT signature genes (3) (Supplemental information 1) to identify classification accuracy of each of the SMaRT signature genes on healthy vs IBD-affected colon tissues (**Fig 1B-*left***). This allowed us to formally define ColAMs in health, as those expressing a core set of 24 genes [2, that are expressed highly in reactive inflammatory (i)ColAMs; 22 that are expressed highly in tolerant non-inflammatory (ni)ColAMs; **Fig 1B-*right***] and in IBD, as those expressing a distinct set of 53 genes (26, that are expressed highly in reactive iColAMs; 27, that are expressed highly in tolerant niColAMs; **Fig 1B-** *right*). It is noteworthy that the brakes and accelerators in health are distinct from IBD (**Fig 1B** *right, see* Supplemental information 2). These genes had AUC values greater than 0.70 (**Fig 1B-*left*,** Supplemental information 2) in discriminating between healthy and IBD-affected colon tissues (including UC and CD, see Supplemental information 2). A KEGG (Kyoto Encyclopedia of Genes and Genomes) pathway enrichment analysis showed that, as expected, model refinement was associated with the enrichment of biological pathways that are more relevant to the gut (Toll-like receptor, nucleotide-binding oligomerization domain containing 2 (NOD2) and TNF signaling; **Fig 1C-D**) with a concomitant de-enrichment of others. When we tested their ability to distinguish healthy from colitis samples, the 53-gene ColAM signature (used independently as 26-gene iColAMs and 27-gene niColAMs) performed consistently better than their corresponding definitions derived from the previously published SMaRT model (3), in both human (H vs. UC/CD; **Fig 1E**) and murine (H vs. dextran sodium sulfate (DSS), a chemical colitogen; **Fig 1F**) datasets. In the case of murine models of DSS-induced acute colitis, we were advantaged by our ability to access a high quality dataset of DSS-colitis murine models representing both acute and chronic phases of colitis (14) which revealed a temporal separation of ColAMs: iColAMs were induced early and persisted throughout the various DSS models, whereas niColAMs were induced exclusively when disease model matched the relapsing remitting nature of IBD, i.e., injury was repetitive in the form of 2 cycles of DSS followed by 3 weeks of recovery/washout (**Fig 1F**).

Non-inflammatory ColAMs in colitis display unique functional coupling between NOD2 and CCDC88A

The earliest and most replicated genetic associations with IBD corresponds to a locus on chromosome 16 that encompasses the *NOD2* gene, with an average allelic odds ratio across multiple studies of 3.1 (15, 16), and its well documented role in the pathogenesis of IBD (4, 17-21). Despite its well documented role in IBD pathogenesis, controversies persist regarding how NOD2 functions and how its risk alleles contribute to colitis, including both UC and CD (21-25). The enrichment of NOD signaling specifically in IBD-associated ColAMs (**Fig 1D**) led us to investigate NOD-centric cellular processes in i/niColAMs. Overlaying i/niColAM gene clusters with physical interactors of NOD1 and NOD2, derived from a prior BioID (Proximity-Dependent Biotin Identification) study (26) revealed a single NOD2-interacting candidate: GIV (a.k.a. Girdin; encoded by gene *CCDC88A*) (**Fig 1G**). Notably, *CCDC88A* is part of the niColAM gene signature, which emerges during the recovery phase of DSS-induced colitis (**Fig 1F**). *CCDC88A* expression positively correlates with *NOD2* (but not *NOD1*) across 21 independent cohorts (**Fig 1H**) and is elevated in UC and CD-associated intestinal macrophages compared to healthy controls (**Fig S1A**).

To validate the functional coupling between NOD2 and CCDC88A in IBD-associated niColAMs, we leveraged a genome-wide siRNA screen in HEK293T cells (27) that measured MDP-induced hyperactivation of NFκB. While NOD2 variants are known to impair bacterial clearance in macrophages and disrupt NFκB activation (18, 27-29), paradoxically, the gut mucosa of IBD patients often shows heightened NFκB activity (30-34). Loss-of-function variants, such as NOD2 *1007fs*, which display 100% penetrance, are consistently associated with CD (35) and impact the severity of disease course in UC (36). Based on these observations, NOD2 is believed to restrict activation of the NFκB pathway by TLR2/4 (37-41) and its dysfunction causes runaway inflammation, thereby increasing the risk of colitis. Consistent with these observations, the functional-genomic screen revealed that among all i/niColAM-genes, depletion of *CCDC88A* within the niColAM cluster (genes presumed to be critical for reducing inflammation) emerged as the most consequential perturbation that increases NFkB activity (**Fig 1I**).

GIV is required for MDP/NOD2-mediated bacterial clearance and controlled inflammation

GIV is a multifunctional signaling scaffold and a prototypical member of the non-receptor Guanine nucleotide Exchange Modulator (GEM) protein family (42). GIV modulates G protein activity downstream of various ligand-activated sensors, including growth factors and integrins (43). Given its recently identified role in modulating macrophage responses (44), we asked if GIV may be a functional modulator of the cytosolic sensor, NOD2. To study the role of GIV in MDP/NOD2-induced inflammatory responses in macrophage *in vitro*, we used 3 cell-based models: (i) GIV-depleted (shGIV) RAW 264.7 murine macrophage cells; this previously-validated cell model displays ~85-90% depletion of GIV protein by immunoblotting (44) (**Fig 2A**)]; (ii) thioglycolate-induced murine peritoneal macrophages (TG-PMs) isolated from myeloid-specific conditional GIV knockout (GIV-KO) mouse, generated previously (44) by crossing Girdin floxed mice to *LysM*cre mice, and confirmed to have ~85-90% depletion of GIV protein (**Fig 2C**); and (iii) THP1 human macrophage lines depleted or not of >~90% GIV protein (by CRISPR; **Fig 2D**).

In GIV-depleted RAW macrophages, MDP/NOD2-induced NFκB activity was significantly elevated (**Fig 2B**), as determined by luciferase reporter assays. These findings were corroborated in HeLa cells (**Fig S1B-C**), commonly used to study NOD2-dependent processes in plasmid transfection settings (45, 46). Briefly, compared to control cells, GIV-depleted HeLa cells (by CRISPR; **Fig S1B**) showed significantly higher MDP/NOD2-induced NFkB activity, confirming the role of GIV in dampening NFkB activity. Consistent with its role in dampening inflammation GIV depletion in TG-PMs led to a ~3-4-fold increase in proinflammatory cytokines [interleukin (IL)1β, IL6, and tumor necrosis factor (TNF)α], as measured by ELISA (**Fig S1D**). Hyper-induction of proinflammatory cytokines was accompanied by a concomitant suppression of the anti-inflammatory cytokine, IL10 (**Fig S1D**). These cytokine profiles were consistent with gene expression patterns assessed via qPCR (**Fig S1E**).

When TG-PMs were infected with Adherent-Invasive *Escherichia coli* strain LF82 (AIEC-LF82), isolated from Crohn's disease (CD) patients (47), GIV-KO TG-PMs exhibited delayed bacterial clearance compared to WT controls (**Fig 2C**). Similarly, GIV-depleted THP1 cells reproduced these findings (**Fig 2E**). Transmission electron microscopy (TEM) confirmed that GIV-KO TG-PMs retained significantly higher numbers of pathogenic AIEC-LF82 bacteria (**Fig 2F-G**).

Tandem mass tag (TMT)-based quantitative proteomics of GIV-depleted RAW macrophages revealed distinct proteomic differences after 16 hours of MDP stimulation (**Fig 2H**). While control cells activated robust NOD2-dependent signaling and inflammasome assembly (**Fig 2I**), GIV-depleted cells showed an acute-phase response and heightened proinflammatory cytokine expression (**Fig 2I**).

These findings establish GIV as a critical regulator of NOD2-driven inflammatory signaling. GIV is essential for maintaining balanced cytokine profiles and facilitating MDP/NOD2-dependent bacterial clearance (**Fig 2J**). In its absence, excessive proinflammatory NFκB signaling occurs, while bacterial clearance is impaired (**Fig 2K**).

GIV-KO mice develop dysbiosis and an exacerbated and protracted *Citrobacter*-induced colitis

To investigate the role of GIV in vivo, we employed a myeloid specific GIV-KO (*Ccdc88a*$^{fl/fl}$/*LysM*^{Cre}) model (see *Methods*) (44). We found that these mice spontaneously develop dysbiosis by ~8-12 wk (**Fig 3A-B**; **Fig S2**). Notably, the strain *Rhizobiales* —uniquely associated with CD patients and absent in healthy controls (P = 0.037) (48) —detected in 100% of GIV-KO mice (5/5) but was undetectable in control littermates (**Fig 3A-B**; **Fig S2**).

Upon *Citrobacter* challenge (**Fig 3C**), GIV-KO mice exhibited an increased acute fecal bacterial load (**Fig 3D**; 1st wk) and an abnormal delay in bacterial clearance, leading to chronic infection (**Fig 3D**; 7th wk). These mice also demonstrated hallmark features of chronic colitis, including colon shortening (**Fig 3E**), patchy transmural inflammation affecting the small intestine, colon, and rectum (**Fig 3F,G**), as well as focal muscle hypertrophy and collagen deposition (**Fig 3H,I**). These findings suggest that GIV in macrophages, and possibly other myeloid cells, plays a critical role in bacterial clearance and the resolution of inflammation during infection.

Protective MDP/NOD2 signaling is abolished in myeloid specific GIV-KO mice.

Prior studies have shown that pre-treatment with MDP ameliorates infection/bacteremia (49, 50), fatality in sepsis (51) and chemical (e.g., trinitrobenzene sulfonic acid, TNBS and DSS)-induced colitis (38); we asked if these protective actions of MDP require GIV. Compared to WT controls, we found that the GIV-KO mice developed significantly worse DSS-induced acute colitis (**Fig 4A**), as determined by disease activity index (**Fig 4B-C**) and histological composite scores accounting for deformation of colon crypts and increased immune infiltration in the colon (**Fig 4D-E**) and; the latter is a composite score of stool consistency, weight loss and the presence of fecal blood (44, 52, 53). Pre-treatment with MDP ameliorated the severity of colitis in WT, but not GIV-KO mice (**Fig 4B-E**). Similar results were seen also in the case of *E. coli*-induced sepsis (**Fig 4F**); fatality was higher in GIV-KO mice compared to WT controls (**Fig 4G**). Pre-treatment with MDP reduced fatality in WT, but not GIV-KO mice (**Fig 4G**). These findings demonstrate that GIV is required for the protective MDP/NOD2 signaling in the setting of infection/inflammation.

Prior studies have shown that MDP priming of NOD2 protects cells from excessive inflammation induced by lipopolysaccharide (LPS) (38, 54). To determine if this protective effect requires GIV, we used GIV-depleted (shGIV) RAW 264.7 murine macrophages and WT controls (shC) to assess NFκB activation following LPS stimulation, with or without MDP pretreatment. In WT cells, MDP pretreatment significantly

reduced NFκB activation, but this protective effect was markedly compromised in GIV-depleted cells (**Fig 4H**). Similar findings were observed in HeLa cells, which express the MD2 co-receptor essential for LPS/TLR4 signaling (46, 55-59) , albeit at low levels (60). In control HeLa cells, MDP pretreatment reduced NFκB activation significantly, both with endogenous NOD2 (**Fig S1F**) and exogenously overexpressed NOD2 (**Fig S1G**). In cells without GIV, this protective effect was either diminished (**Fig S1F**) or virtually abolished (**Fig S1G**). Additionally, when MDP-primed TG-PMs were infected with the pathogenic AIEC-LF82 strain (47), MDP treatment accelerated bacterial clearance in WT cells but not in KO PMs (**Fig 4I-J**).

These findings demonstrate that GIV is essential for protective MDP/NOD2 signaling, which counteracts LPS/TLR4-driven proinflammatory NFκB signaling (**Fig 4K**). Without GIV, NFκB signaling becomes excessive, and bacterial clearance is delayed and impaired (**Fig 4L**).

MDP/NOD2 signaling differentially modulates ColAM populations in WT and GIV-KO mice

Publicly available datasets of DSS-induced colitis, encompassing acute, chronic, and recovery phases (**Fig 5A, Fig 1F**), reveal that iColAMs are upregulated during the acute phase but decrease in the chronic and recovery phases (**Fig 5B** *left*). Conversely, niColAMs are diminished during the acute phase but increase during the chronic and recovery phases (**Fig 5B** *right*). Because GIV is required for the protective effects of MDP/NOD2 signaling in DSS-induced colitis (**Fig 4A-E**), we investigated whether this protection involves GIV/MDP/NOD2 modulation of iColAM and niColAM populations.

To address this, we analyzed colon transcriptomic data from WT and GIV-KO mice treated with DSS-colitis, with or without MDP treatment (**Fig 5C**). A composite score of niColAMs effectively distinguished MDP-treated WT colon tissues from WT controls (classification accuracy = 1) (**Fig 5D**). Similarly, a composite score of iColAMs segregated MDP-treated GIV-KO colon tissues from GIV-KO controls (classification accuracy = 1) (**Fig 5D**). These findings demonstrate that MDP treatment upregulates healing niColAM populations in WT mice, earlier than expected (**Fig 5B** *right*), perhaps fueling early recovery from DSS-induced colitis; however, MDP treatment in GIV-KO mice increases inflammatory iColAMs, exacerbating disease severity (**Fig 4A-E** and **5E**). Gene Ontology (GO) analysis of differentially expressed genes further supports these observations, indicating protective and healing responses in MDP-treated WT mice but not in GIV-KO mice compared to their respective controls (**Fig 5F-I**, see **Supplemental information 3** for a differentially expressed genes list). Bulk RNA sequencing deconvolution confirmed that the identified iColAM and niColAM populations closely align with conventional M1 (pro-inflammatory) and M2 (anti-inflammatory) polarized macrophage states (**Fig 5J, K**).

These results highlight that GIV is essential for MDP/NOD2-induced protective effects *in vivo*, serving uniquely the healing niColAM macrophage populations that are critical for balancing the actions of iColAM macrophage and restoring tissue homeostasis.

The GIV●NOD2 interaction is direct and dynamically regulated by MDP

NOD2 typically exists in an inactive, ADP-bound conformation stabilized by intramolecular interactions; upon binding to MDP, NOD2 undergoes conformational changes that facilitate ADP-to-ATP exchange, self-oligomerization, and downstream signaling (61, 62) (**Fig 6A**).

We asked if GIV physically interacts with NOD2. We found that GIV co-immunoprecipitated with NOD2 (**Fig 6B**), indicating that the two full length endogenous proteins interact in cells. *In situ* proximity ligation assay (PLA on endogenous, full-length proteins; **Fig 6C**) showed that this interaction is augmented by ligand (MDP) stimulation, and that the assembly of GIV●NOD2 complexes peak at ~1 h post-stimulation (**Fig 6D-E**). Co-immunoprecipitation assays with exogenously expressed tagged proteins further validated this interaction across various time points after MDP stimulation. Using HA-NOD2 or GIV-FLAG as bait, we detected the assembly of GIV●NOD2 complexes within ~1-3 h, before their disassembly by ~6 h post-stimulation (**Fig 6F, Fig S3A**). This temporal pattern was consistent regardless of bait-prey pairing, confirming the dynamic regulation of the GIV●NOD2 interaction by MDP (**Fig 6F, Fig S3A**).

To resolve the ultrastructural nature of the subcellular compartments where the GIV●NOD2 complexes are assembled, we performed immunogold labeling followed by electron microscopy on MDP-stimulated (1h) TG-PMs using antibodies against GIV (large particles, 18 nm) and NOD2 (small particles, 12 nm). Notably, NOD2 colocalized with membrane-associated GIV, predominantly on actin strands (**Fig 6H-L**), within particle-rich cytoplasmic structures (63) (PaCS; which contain polyubiquitinated proteins and proteasomes) (**Fig 6H, J**) and around swollen mitochondria with abnormal morphology (**Fig 6M**). Findings indicate that the NOD2●GIV interaction is augmented by MDP and is associated with the membrane and cytoskeletal elements, supporting its potential role in NOD2-mediated signaling and cellular responses (64).

The C-terminus of GIV directly binds the LRR domain of NOD2

GIV is a large, multimodular scaffold protein (1871 amino acids) with several interaction domains (**Fig 7A**), NOD2, on the other hand, consists of three major domains: CARD, NBD, and LRR (**Fig 7B**). While NOD1 and NOD2 share structural similarities, co-immunoprecipitation analyses revealed that GIV specifically binds to NOD2 but not NOD1 (**Fig 7C, D**), indicating that the GIV●NOD2 interaction is specific. Because the ~210 amino acid C-terminal (CT) module of GIV consistently couples to diverse receptors and sensors via short linear motifs (SLIMs) (**Fig 7A**), we asked if this region is sufficient for NOD2 binding. Indeed, GIV-CT was sufficient to bind NOD2 (**Fig S3B,** *right*), but it did not interact with NOD1 (**Fig S3B,** *left*).

To identify the specific domain of NOD2 responsible for the GIV●NOD2 interaction, we performed co-immunoprecipitation experiments using NOD2 deletion mutants lacking the CARD domains (ΔCARD), NBD (ΔNBD), or LRR (ΔLRR) domains (**Fig 7E, F**), we found that GIV binding to NOD2 is independent of the CARD and NBD domains; instead, the interaction is mediated by the LRR domain of NOD2 (**Fig 7G, S3C-D**) and deletion of the terminal repeat in the LRR domain (del Δ) virtually abolished GIV binding (**Fig 7D,G**). Co-immunoprecipitation (**Fig S3E**) and GST-pulldown studies with GIV-CT (**Fig 7I**, **Fig S3F**) corroborated these findings. Furthermore, mutagenesis of key arginine residues in NOD2 (R1034 and R1037) (**Fig 7D)**, which stabilize its terminal LRR (**Fig 7H)**, significantly reduced binding (**Fig 7I**). These findings collectively demonstrate that the terminal LRR repeat of NOD2 is essential for its interaction with the C-terminal region of GIV (**Fig 7D, H, I**), providing insights into the molecular basis of their functional coupling.

GIV cannot bind the CD-risk NOD2 *1007fs* variant, which lacks terminal LRR

We next investigated whether GIV binding is affected by CD-associated NOD2 variants (*R702W*, *G908R* and *1007fs*) which collectively account for ~80% of mutations associated with CD susceptibility (**Fig 8A**) (21, 65). These variants affect amino acids located proximal to or within the LRR domain (**Fig 8B**). Binding to GIV was impaired in two variants, R702W and *1007fs* (**Fig 8C**) both of which exhibit high disease penetrance (~100%; **Supplementary Table 1**). By contrast, the G908R variant, which affects the MDP-contact site (66, 67) retained binding to GIV at levels comparable to NOD2-WT (**Fig 8C**). Further studies confirmed that the *1007fs* variant remains deficient in GIV binding even upon MDP stimulation (**Fig 8D**).

We next analyzed the response of NOD2 CD-risk variants to LPS stimulation following MDP pretreatment to assess the role of GIV in modulating this response. Using NFκB luciferase assays in cells with or without GIV, we found that MDP pretreatment significantly suppressed LPS-induced NFκB activation in the presence of NOD2-WT (**Fig 8E**); However, this protective effect was impaired in cells expressing the NOD2 variants (**Fig 8E**; red *p*-values). For instance, while NOD2-WT conferred ~65% protection, the NOD2-*1007fs* variant, which cannot bind GIV, showed only ~20% protection (**Fig 8E**). In GIV-KO cells, the degree of suppression by NOD2-WT was reduced from ~65% to ~10% (**Fig 8E**; gray *p*-values). The residual ~10–20% suppression observed in settings where GIV cannot bind NOD2 (e.g., in GIV-KO cells or with the NOD2-*1007fs* variant) suggests the existence of potential GIV-independent mechanisms or contributions from endogenous NOD2 in the cells. These findings underscore that the GIV●NOD2 interaction is critical for a significant portion of the protective effects of MDP signaling. Disruption of this interaction in patients carrying the *1007fs* CD-risk variant (or other binding-deficient mutants) likely plays a pivotal role in exacerbating runaway inflammation (LPS-induced NFκB activation) and undermining efforts to restore intestinal homeostasis (**Fig 8F-G)**.

DISCUSSION

The major discoveries we report here are threefold. First, we identified a core set of genes within a stringent gene signature that formally defines colon-associated inflammatory and non-inflammatory macrophage, in both health and IBD. We established GIV as a critical physical and functional interactor of NOD2, enabling protective and homeostatic NOD2 signaling in non-inflammatory macrophage. This protective mechanism operates within the lamina propria of the gut across acute (DSS-induced colitis), chronic (IBD), and acute sepsis settings. Third, we elucidated the molecular mechanisms underlying GIV's direct and dynamic interaction with NOD2. This interaction plays a dual role when macrophage sense bacteria and/or bacterial products (**Fig 8F-G**): (i) suppressing NFκB-dependent inflammatory signals, and (ii) simultaneously enhancing anti-bacterial pathways and processes that operate independently of NFκB. Together, these dual functions safeguard the host by preventing excessive inflammation while ensuring effective microbial clearance. Finally, our findings unexpectedly pinpointed a molecular basis for the most consequential loss-of-function CD risk variant, i.e.,*1007fs*; in the colitic dysbiotic gut environment, where NOD2 plays a pivotal role in controlling inflammation and microbial clearance, the inability of GIV to bind the NOD2-*1007fs* variant provides concrete mechanistic insight into how this risk allele contributes to persistent inflammation and disease pathology. Insights gained spur new paradigms in innate sensing and signaling via NOD2 in the following ways.

Machine learning-assisted definitions provide a framework for studying macrophage populations in the gut. The ColAM signatures identified in this study demonstrate their utility as computational tools, independently distinguishing colon-associated reactive and tolerant macrophage states, enriched in signaling pathways linked to colitis. ColAMs, a subset of the broader SMaRT gene signature (338 genes), represent unbiased markers of macrophage activation observed in both transcriptomic and proteomic analyses. This subset remains clinically meaningful and relevant. The colitis-associated 53-gene signature within ColAMs identifies distinct states of macrophage populations (reactive/inflammatory vs. tolerant/non-inflammatory macrophages) in colitis tissues, markedly different from healthy colon tissue. The fact that the IBD-ColAM signatures enriched gut-relevant pathways and can be applied to identify macrophage functional states in bulk-seq datasets, is a testimony to their specificity and accuracy as computational tools and represent.

In the healthy gut, the predominance of niColAM-associated macrophages may reflect the gut's need to maintain homeostasis amidst a dense microbial environment separated from immune cells by a single epithelial layer. Tonic activation of niColAMs likely protects crypt stem cells and the enteric nervous system from collateral damage caused by inflammatory responses, functioning akin to "parking brakes" that maintain a low-grade surveillance mode. By contrast, during chronic inflammation and dysbiosis, iColAMs act as "accelerators," while niColAMs function as robust "brakes" to prevent runaway inflammation. Dysfunctional macrophage states—such as overactive iColAMs (jammed in an "accelerator" state) or failed niColAMs (non-functional "brakes")—may contribute to gut dysbiosis and chronic inflammation. These findings highlight a dynamic interplay between macrophage subtypes, forming a regulatory framework where "brakes" and "accelerators" cooperate to maintain tissue homeostasis at the mucosal barrier. Malfunction in this balance

may underpin pathological conditions such as colitis, offering new insights into disease mechanisms and potential therapeutic targets.

GIV enhances 'brake'-like non-inflammatory NOD2 functions in macrophages

We show that *CCDC88A* is the only molecule among the 53-gene IBD-ColAM signature that functionally and physically interacts with NOD2 to serve key non-inflammatory actions of niColAMs. NOD2-mediated suppression of NFκB is a crucial but poorly understood protective mechanism (28). NOD2 also facilitates bacterial clearance by coordinating cytoskeletal, organellar, and signaling processes. Here, we demonstrate that GIV binding to NOD2 is critical for both arms of this protective response: (i) measured suppression of NFκB-dependent inflammation optimal for immunity and homeostasis, and (ii) enhanced anti-bacterial pathways independent of NFκB. Without GIV, NOD2's protective functions are compromised, microbes are not efficiently cleared, and macrophages assume a reactive phenotype.

These findings align with prior studies showing GIV as a "brake" within the LPS/TLR4 signaling cascade (44). GIV's conserved C-terminal motif binds and dampens inflammatory signaling by TLR1/2, TLR2/6, and TLR3, inducing tolerogenic programs aimed at homeostasis and immunity (44). Thus, GIV emerges as a point of convergence for major pattern recognition receptors (PRRs), coordinating early host defense against pathogens (26, 44, 68). Whether GIV serves as a platform for crosstalk between the two PRRs requires further dissection.

The GIV●NOD2 interaction couples NOD2 to other signaling domains and pathways

Our findings reveal that the GIV●NOD2 interaction is specific, direct, and dynamically regulated by MDP. Binding is mediated via GIV's C-terminal ~210 amino acids and the terminal LRR repeat of NOD2. This makes GIV the 3rd such interactor of NOD2-LRR (only 2 prior) (69), of which only one prior was shown to suppresses NFκB and augment protective signaling. Although we define how GIV impacts NOD2 signaling, its potential reciprocal regulation remains unexplored. Given that high cAMP levels promote NOD2-mediated microbial clearance (70, 71), the GIV●NOD2 interaction might relieve GIV-dependent cAMP inhibition (via Gi activation and Gs inhibition) (72). This would position NOD2 as another receptor modulating trimeric G-proteins and cAMP through GIV's C-terminal SLIM motifs, joining a lengthy list of priors (43). Future studies will identify the specific SLIM mediating this interaction and investigate overlap with motifs for TLR4 or Gαi/s binding.

Loss of NOD2●GIV interaction is a feature of the 1007fs CD-risk variant

The three main CD-associated variants (*R702W*, *G908R*, and *1007fs*) interfere with bacterial recognition (73). While G908R's defect lies in impaired MDP contact (66, 67), R702W and 1007fs show defects in palmitoylation and PM localization (26). Only the *1007fs* variant, which lacks the terminal LRR repeat, fails to regain functionality upon restoring PM localization (74), indicating that *1007fs* variant lacks key functions, perhaps because of the truncated terminal LRR repeat. We show that the *1007fs* variant does not bind GIV and that it lacks the same terminal LRR repeat that is essential for the NOD2●GIV interaction. Because the

our conclusions are supported by both co-immunoprecipitation and *in vitro* pulldown assays using recombinant NOD2-LRR proteins, it is unlikely that loss of GIV binding we observe in co-immunoprecipitation studies is merely a consequence of protein mis-localization in cells [as implicated previously for other NOD2-interactors, e.g., Erbin (75)]. Thus, GIV emerges as a first-in-class NOD2-interactor that requires the 10th LRR repeat, which is lost in the *1007fs* variant. Because this variant (also termed *3020insC*) is most consistently associated with CD across multiple studies and population groups , and displays 100% disease penetrance, it is not surprising that our GIV-KO animals challenged with *Citrobacter* develop key features of CD, e.g., patchy ileocolitis with transmural inflammation, focal muscle hypertrophy and fibrosis, and dysbiosis with defective bacterial clearance. It is noteworthy that these developed within 7 wks, which is relatively early compared to the only other known murine model of CD SAMP1/YitFcs, which takes ~30 wks (76). The latter develop CD-like spontaneous ileitis, via genetic defects in many genes, e.g., *Pparg, Nod2, Il10ra*, among others. Future studies will assess whether *Citrobacter*-challenged GIV-KO mice progress to recapitulate some or most features of CD at a molecular (defective innate and adaptive immune response) and phenotypic (develop fistula) level.

LIMITATIONS OF STUDY

Although all phenotypes were assessed in the context of MDP stimulation, ensuring NOD2-specificity in the experimental readouts and conclusions, the importance of the GIV●NOD2 interaction in the phenotypes could not be interrogated due to the lack of specific tools. Future investigations will require the identification of binding-deficient mutants of GIV and/or NOD2 to directly assess the interaction's functional significance. The observation that the GIV●NOD2 interaction is significantly enhanced by MDP raises the possibility that additional factors, such as pH, ATP levels, and spatial or temporal segregation of interacting proteins, might also regulate this interaction. These factors are known to influence NOD2's interactome and functional outcomes but were not explored in this study. Additional studies are necessary to further dissect these complex relationships and to provide a more comprehensive understanding of the mechanisms at play.

METHODS

Computational

StepMiner analysis

StepMiner is an algorithm that identifies step-wise transitions using step function in time-series data (77). StepMiner undergoes an adaptive regression scheme to verify the best possible up and down steps based on sum-of-square errors. The steps are placed between time points at the sharpest change between expression levels, which gives us the information about timing of the gene expression-switching event. To fit a step function, the algorithm evaluates all possible steps for each position and computes the average of the values on both sides of a step for the constant segments. An adaptive regression scheme is used that chooses the step positions that minimize the square error with the fitted data. Finally, a regression test statistic is computed as follows:

$$F\ stat = \frac{\sum_{i=1}^{n}(\widehat{X}_i - \bar{X})^2/(m-1)}{\sum_{i=1}^{n}(X_i - \widehat{X}_i)^2/(n-m)}$$

Where X_i for $i = 1$ to n are the values, $\widehat{X}_i$ for $i = 1$ to n are fitted values. m is the degrees of freedom used for the adaptive regression analysis. $\bar{X}$ is the average of all the values: $\bar{X} = \frac{1}{n} * \sum_{j=1}^{n} X_j$. For a step position at k, the fitted values $\widehat{X}_l$ are computed by using $\frac{1}{k} * \sum_{j=1}^{n} X_j$ for $i = 1$ to k and $\frac{1}{(n-k)} * \sum_{j=k+1}^{n} X_j$ for $i = k+1$ to n.

Measurement of classification strength or prediction accuracy:

To measure the strength of classification or prediction accuracy, Receiver Operating Characteristic (ROC) curves were generated for each gene. These curves illustrate the diagnostic ability of a binary classifier system (e.g., high vs. low StepMiner normalized gene expression levels) as its discrimination threshold is adjusted along with the sample order. ROC curves plot the True Positive Rate (TPR) against the False Positive Rate (FPR) at various threshold settings. The Area Under the Curve (AUC) quantifies the probability that a classifier will correctly rank randomly chosen samples into two groups of healthy and IBD patients. Alongside ROC AUC, other classification metrics such as accuracy ((TP + TN)/N; TP: True Positive; TN: True Negative; N: Total Number), precision (TP/(TP+FP); FP: False Positive), recall (TP/(TP+FN); FN: False Negative), and f1 score (2 * (precision * recall)/(precision + recall)) were computed. The Python Scikit-learn package was used to calculate the ROC-AUC values.

Composite gene signature analysis using Boolean Network Explorer (BoNE)

Boolean network explorer (BoNE) (7) provides an integrated platform for the construction, visualization and querying of a gene expression signature underlying a disease or a biological process in three steps: First, the expression levels of all genes in these datasets were converted to binary values (high or low) using the StepMiner algorithm. Second, Gene expression values were normalized according to a modified Z-score approach centered around *StepMiner* threshold (formula = (expr - SThr)/3*stddev). Third, the normalized expression values for every gene were added together to create the final composite score for the gene signature. These composite scores represent the overall activity or state of biological pathways associated

with the genes and, hence, can identify differences between control and query groups *within* any given dataset. However, composite scores can neither be directly compared between various gene signatures on a dataset (because they are not normalized according to the number of genes in each signature), nor can the same signature be compared across datasets (which are individually normalized according to intra-dataset sample distribution or have other inherent differences). The samples were ordered based on the final signature score. Differentially expressed genes were identified using DESeq2 R package. Welch's Two Sample t-test (unpaired, unequal variance (equal_var=False), and unequal sample size) parameters were used to compare the differential signature score in different sample categories. Violin, swarm and bubble plots are created using python seaborn package version 0.10.1. Pathway enrichment analyses for genes were carried out using the KEGG database (78). Violin plots are created using python seaborn package version 0.10.1.

Correlation Heatmap

The correlation coefficient between two gene expression values in a transcriptomics dataset was calculated by plotting them in a scatter plot and measuring the correlation coefficient using Python's SciPy library.

Bulk RNAseq Deconvolution

The *in-silico* deconvolution of bulk RNA sequencing data to estimate immune cell-type abundance in murine colon samples was performed using the Granulator R package (PMID: 33159064). To normalize cell-type abundances, we utilized the immune cell signature matrix developed by Monaco et al. (PMID: 30726743) (79).

Experimental

Cell culture

Thioglycolate-elicited murine peritoneal macrophages (TGPMs) were collected from peritoneal lavage of 8- to 12-wk-old C57BL/6 mice with ice cold RPMI (10 ml per mouse) 4 days after intraperitoneal injection of 3 ml of aged, sterile 3% thioglycolate broth (BD Difco, USA) and cultured as described previously (80). Cells were passed through 70 µm filter to remove possible tissue debris contamination during harvesting. Cells were counted, centrifuged, and resuspended in RPMI-1640 containing 10 % FBS and 1% penicillin/streptomycin. Cells were plated with required cell density and the media was changed after 4 h to remove non adherent cells. Cells were allowed to adjust to overnight culture before the addition of stimuli as indicated in the figure legends. RAW264.7, HEK293T and HeLa cells (from ATCC) were maintained in the DMEM media containing 10% FBS and 1% penicillin/streptomycin.

Bacteria and bacterial culture

Citrobacter rodentium (strain DBS100) and Adherent Invasive *Escherichia coli* strain LF82 (AIEC-LF82) were cultured from a single colony inoculation into LB broth for 6-8 h on shaking incubator, followed by overnight

culture under oxygen-limiting conditions, without shaking, to maintain their pathogenicity as done previously (81-83). Bacterial cells were counted by measuring an absorbance at 600 nm (OD600), washed with PBS, and infected with indicated MOI in figure legends.

Mice

Ccdc88a$^{fl/fl}$ mice were a gift from Dr. Masahide Takahashi (Nagoya University, Japan) and was developed as described (84). LysM$^{Cre/Cre}$ mice (B6.129P2-Lyz2t (79)(cre)Ifo/j) were purchased from the Jackson Laboratory. *Ccdc88a*$^{fl/fl}$ x LysM$^{Cre/-}$ mice were generated previously by us as described (44) and were maintained as homozygous floxed and heterozygous LysMcre. Primers required for genotyping are mentioned in primer table. Both male and female mice (8-12 weeks) were used and maintained in an institutional animal care at the University of California San Diego animal facility on a 12-hour/12-hour light/dark cycle (humidity 30–70% and room temperature controlled between 68–75 °F) with free access to normal chow food and water. All mice studies were approved by the University of California, San Diego Institutional Animal Care and Use Committee (IACUC).

Fecal pellet collection, DNA extraction and 16S rRNA sequencing

Individual mice fecal pellets from co-housed GIV-KO mice and their littermate WT controls (8-12 weeks) were collected in clean containers and frozen at -80ºC untill use. Samples were transported to microbiome core facility, University of California, San Diego for 16S rRNA processing. Total DNA was extracted from the individual mice fecal pellets using MagMAX Microbiome Ultra Nucleic Acid Isolation kit, (Thermo Fisher Scientific, USA) and automated on KingFisher Flex robots (Thermo Fisher Scientific, USA). 16S rRNA gene amplification was performed according to the Earth Microbiome Project protocol (85). Briefly, Illumina primers with unique forward primer barcodes (86) were used to amplify the V4 region of the 16S rRNA gene (515F-806R (87)) with single reactions per sample (88). Equal volumes of each amplicon were pooled, and the library was sequenced on the Illumina MiSeq sequencing platform with paired-end 150 bp cycles.

16S rRNA gene data analysis

QIIME2 (89) was used to process the demultiplexed files. Sequences were filtered, denoised and trimmed to 150 bp using DADA2 (90), which is used to correct Illumina-sequenced amplicon errors. The sequences were classified using the q2-feature-classifier plugin from QIIME2 that was trained on the Green genes 13_5 99% OTUs trimmed to 150 bp. [Sentence about correlation analysis.] Alpha and beta diversity plots were generated using the R microbiome package (91). Alpha diversity was estimated using Faith's phylogenetic diversity and Shannon diversity. Beta diversity was estimated using Non-Metric Multidimensional Scaling (NMDS) and Bray-Curtis dissimilarity (91).

***C. rodentium* induced infectious colitis**

C. rodentium (strain DBS100) induced infectious colitis studies were performed on 8-week-*old* GIV-KO and their littermate WT control mice. *C. rodentium* were grown overnight in LB broth with shaking at 37 ºC. Mice

were gavaged orally with 5 x 10^8 CFU in 0.1 ml of PBS (92, 93). To determine viable bacterial numbers in faeces, fecal pellets were collected from individual mice, homogenized in ice-cold PBS, serially diluted, and plated on MacConkey agar plates. Number of CFU was determined after overnight incubation at 37 ºC. Colon samples were collected to assess histology in the 7th week.

DSS-induced colitis

To induce colitis, mice were fed with drinking water containing 2.5% dextran sulfate sodium (DSS, w/v) (MP Biomedicals, MW 36–50 kDa) for five days and then replaced normal drinking water as described (94, 95). For treatment study, MDP (100 mg/mouse/day) was administered via intraperitoneal route in 100 ml total volume sterile saline every alternate day starting from day 0 of experiment. Mice were sacrificed on the 14th day, and colon length was assessed. Colon samples were collected for assessing gene expression the levels of mRNA (by qPCR). Drinking water levels were monitored to determine the volume of water consumption. Weight loss, stool consistency, and fecal blood were recorded fro individual animals, and these parameters were used to calculate an average Disease Activity Index (DAI) as described previously (96). Colon histology was assessed in hematoxylin and eosin-stained tissue sections using standard protocols.

***E. coli*-induced sepsis**

E. coli (strain RS218) was grown overnight in Lysogeny broth (LB) media with shaking at 37ºC. Next morning, fresh LB media was used to dilute cultures to 1:50 and grow up to mid-log phase, washed twice with PBS, and reconstituted in PBS. GIV-KO mice (8–12-week-old) and their control WT littermates were injected with 1.5 x 10^8 CFU of *E. coli* in 200 ul and mice survival was recorded for 24h post-infection. Mice were pre-treated with MDP (100 µg i.p.) or PBS 18 h before the infection.

Transmission electron microscopy (TEM) and immunogold EM staining

Cells were fixed with Glutaraldehyde in 0.1M Sodium Cacodylate Buffer, (pH 7.4) and post-fixed with 1% OsO4 in 0.1 M cacodylate buffer for 1 hr on ice. The cells were stained with 2% uranyl acetate for 1 hr on ice and dehydrated in graded series of ethanol (50-100%) while remaining on ice. The cells were washed once with 100% ethanol and twice with acetone (10 min each) and embedded with Durcupan. Sections were cut at 60 nm on a Leica UCT ultramicrotome and picked up on 300 mesh copper grids. All sections were post-stained sequentially 5 min with 2% uranyl acetate and 1 min with Sato's lead stain. Samples were visualised using JEOL 1400 plus equipped with a bottom-mount Gatan OneView (4k x 4k) camera. For immunogold staining to determine co-localization of NOD2 and GIV. The sections were incubated with mouse anti-NOD2 antibody (Santa Cruz, sc-56168, 1:50 dilution) and rabbit anti-GIV antibody (Millipore sigma, ABT80; 1:50 dilution) followed by secondary antibodies 18 nm colloidal gold of donkey anti-rabbit IgG and 12 nm gold of donkey anti-mouse IgG (Jackson ImmunoResearch Laboratories, Inc.). Samples were visualised using JEOL 1400 plus equipped with a bottom-mount Gatan OneView (4k x 4k) camera.

Plasmid constructs

The plasmids used in this study were HA-Nod1 and HA-Nod2 (from Dana Philpott (97) and M. D'Amato (98)); and His-Myc tagged NOD2 constructs (His-myc-Nod2 FL, ΔCARD-His-myc-Nod2, ΔNBD-His-myc-Nod2, ΔLRR-His-myc-Nod2) were generous gift from Santanu Bose (99), . All other Nod2 mutants were generated by site directed mutagenesis. GST-Nod2-LRR and Myc-Nod2 were cloned into pGEX-6P and pCMV-myc vectors, respectively, using cloning sites indicated in Key Resource Table.

Protein expression and purification

GST and His-tagged proteins were expressed in *E. coli* strain BL21 (DE3) and proteins were purified as described (44, 100, 101). Briefly, to stimulate protein expression, bacteria cultures were activated with 1 mM IPTG overnight at 25°C. Bacteria were then pelleted and resuspended in either GST lysis buffer (25 mM Tris-HCL (pH 7.4), 20 mM NaCl, 1 mM EDTA, 20% (vol/vol) glycerol, 1% (vol/vol) Triton X-100, protease inhibitor cocktail) or His lysis buffer (50 mM NaH2PO4 (pH7.4), 300 mM NaCl, 10 mM imidazole, 1% (vol/vol) Triton-X-100, protease inhibitor cocktail), sonicated and lysates were cleared by centrifugation at 12,000 x g at 4°C for 30 mins. Supernatant was then affinity purified using glutathione-Sepharose 4B beads or HisPur Cobalt Resin, followed by elution, overnight dialysis in PBS, and then stored at -80°C until use.

Transfection, lysis, and quantitative immunoblotting

HEK293T and HeLa cells were cultured in DMEM media containing 10% FBS and antibiotics according to the ATCC guidelines. Cells were transfected using polyethylenimine for DNA plasmids following the manufacturers' protocols. Lysates for immunoprecipitation assays were prepared by resuspending cells in lysis buffer (20 mM HEPES, pH 7.2, 5 mM Mg-acetate, 125 mM K-acetate, 0.4% Triton X-100, 1 mM DTT) supplemented with 500 μM sodium orthovanadate, phosphatase inhibitor cocktails (Sigma) and protease inhibitor cocktails (Roche), and cleared (10,000 x *g* for 10 min) before use. For immunoblotting, proteins were fractionated by SDS-PAGE and transferred to PVDF membranes (Millipore). Membranes were blocked with 5% nonfat milk dissolved in PBS before incubation with primary antibodies followed by detection with secondary antibodies using infrared imaging with two-color detection and quantification were performed using a Li-Cor Odyssey imaging system. All Odyssey images were processed using Image J software (NIH) and assembled for presentation using Photoshop and Illustrator software (Adobe).

Immunoprecipitation, *in vitro* GST-pulldown with recombinant purified protein or cell lysates

For *in vitro* pulldown assays, purified GST-tagged proteins from *E. coli* were immobilized onto glutathione Sepharose beads by incubating with binding buffer (50 mM Tris-HCl (pH 7.4), 100 mM NaCl, 0.4% (vol/vol) Nonidet P-40, 10 mM MgCl2, 5 mM EDTA, 2 mM DTT) overnight at 4°C with continuous rotation. GST-protein bound beads were washed and incubated with purified His-tagged proteins resuspended in binding buffer or with pre-cleared (by centrifugation at 10,000xg for 10 min) cell lysates prepared using lysis buffer [20 mM HEPES, pH 7.2, 5 mM Mg-acetate, 125 mM K-acetate, 0.4% Triton X-100, 1 mM DTT, 500 μM sodium orthovanadate supplemented with phosphatase inhibitor cocktail (Sigma Aldrich) and protease inhibitor cocktail (Roche)] for 4 hrs at 4°C. After binding, bound complexes were washed four times with 1 ml

phosphate wash buffer (4.3 mM Na2 HPO4, 1.4 mM KH2PO4 (pH 7.4), 137 mM NaCl, 2.7 mM KCl, 0.1% (vol/vol) Tween-20, 10 mM MgCl2, 5 mM EDTA, 2 mM DTT, 0.5 mM sodium orthovanadate) and eluted by boiling in Laemmli buffer (5% SDS, 156 mM Tris-Base, 25% glycerol, 0.025% bromophenol blue, 25% β-mercaptoethanol).

Co-immunoprecipitation assays

N-terminal HA- or Myc-tagged NOD2 and C-terminal FLAG-tagged GIV full length proteins were co-expressed in HEK293T cells and 48 h after transfection, cells were stimulated with 10 µg/ml MDP (L18-MDP, Invivogen) for 1, 3 and 6 h followed by cell lysis in lysis buffer (20 mM HEPES, pH 7.2, 5 mM Mg-acetate, 125 mM K-acetate, 0.4% Triton X-100, 1 mM DTT, 0.5 mM sodium orthovanadate, Tyr phosphatase inhibitor cocktail, Ser/Thr phosphatase inhibitor cocktail, and protease inhibitor cocktail). For immunoprecipitation, equal aliquots of clarified cell lysates were incubated for 3h at 4°C with 2 µg of appropriate antibody [either anti-HA mAb or anti-FLAG M2Ab (Sigma Monoclonal ANTI-FLAG® M2, Clone M2)]. Subsequently, protein G Sepharose beads (GE Healthcare; 40 µl 50% v:v slurry) were added and incubated at 4°C for an additional 60 min. Beads were washed 4 times (1 ml volume each wash) in PBS-T buffer [4.3 mM Na2HPO4, 1.4 mM KH2PO4, pH 7.4, 137 mM NaCl, 2.7 mM KCl, 0.1% (v:v) Tween 20, 10 mM MgCl2, 5 mM EDTA, 2 mM DTT, 0.5 mM sodium orthovanadate] and immune complexes were eluted by boiling in Laemmli's sample buffer. Bound immune complexes were separated on SDS PAGE and analyzed by immunoblotting with anti-HA, anti-Myc and anti-FLAG antibodies. In assays where the impact of nucleotides was studied on protein-protein interactions, cells were were first permeabilized with 4 µg/ml of streptolysin-O (Sigma-Aldrich, Budapest, Hungary) for 30 min at 37°C followed by incubation with nucleotides (ADP, ATP, or ATPgS).

Proximity ligation assay (PLA)

THP1 cells grown on glass coverslips nearly 70% confluency, washed two times with PBS, and fixed 20 min at room temperature with 4% (wt/vol) PFA. After washing with PBS, cells were processed for PLA using the Duolink *In Situ* PLA kit according to the manufacturer's instructions. Briefly, coverslips were blocked for 1 hour at room temperature, followed by a 1-hour incubation with primary antibodies targeting GIV and NOD2. Subsequently, cells were incubated with PLA probes for 1 hour in a humidified chamber at 37°C. If the two oligo probes are in proximity, ligation occurs, and further amplification steps enable fluorescence detection of the reaction as bright red dots (566–594 nm). Cells were then counterstained with DAPI to visualize nuclei and imaged using Cytation10 widefield microscopy or leica stellaris confocal. Quantification of PLA dots were performed using Gen5 or ImageJ software.

Confocal immunofluorescence

Cells were fixed with 4% paraformaldehyde in PBS for 30 min at room temperature, treated with 0.1 M glycine for 10 min, and subsequently blocked/permeabilized with blocking buffer (PBS containing 1% BSA and 0.1% Triton X-100) for 20 min at room temperature. Primary and secondary antibodies were incubated for 1 h at room temperature or overnight in blocking buffer. Dilutions of antibodies used were as follows: HA (1:200)

and DAPI (1:1000). Alexa fluor fluorescent dye conjugated secondary antibodies were used at 1:500 dilutions. For visualizing actin organizations cells were stained with 16 mM Phalloidin Alexa Fluor™-594 for 30 min at room temperature, washed three times with PBS. ProLong Glass antifade reagent is used for mounting the coverslips on glass slides.

NFκB reporter assay

RAW 264.7 cells (50000 cells/well in 96-well plate) were transfected together with 50 ng NFκB reporter plasmid and 5 ng Renilla luciferase control plasmid. After 24h, cells were stimulated with L18-MPD (10 µg/ml) for 6 hr and NFκB activity was assessed using the Dual-luciferase Reporter Assay System using manufacturers protocol. For HeLa cells 10000 cells/well in 96-well plate were seeded and transfected with 25 ng NFκB reporter plasmid, 0.5 ng Renilla luciferase control plasmid and either 5 ng/well of NOD2-WT or its mutants. Cells were primed with or without L18-MPD (10 µg/ml) for 16 hr before stimulating with LPS100ng/ml for 6h and NFκB activity was assessed using a noncommercial dual luciferase enzyme assay as described (102).

RNA extraction and Quantitative PCR

Total RNA was isolated using TRIzol reagent (Life Technologies) and Quick-RNA MiniPrep Kit (Zymo Research, USA) as per manufacturer's guidelines. RNA was converted into cDNA using the qScript™ cDNA SuperMix (Quantabio) and quantitative RT-PCR (qPCR) was carried out using PowerUp™ SYBR™ green master mix (Applied Biosystems, USA) with the StepOnePlus Quantitative platform (Life Technologies, USA). The cycle threshold (Ct) of target genes was normalized to 18S rRNA gene and the fold change in the mRNA expression was determined using the 2^-ΔΔCt method.

Gentamicin Protection Assay

Gentamicin protection assay was used to quantify viable intracellular bacteria as described previously (81). Approximately, 2×10^5 TGPMs were seeded into 12-well culture dishes overnight before infection at an MOI of 10 for 1 h in antibiotic-free RPMI media containing 10% FBS in a 37 °C CO2 incubator. Cells were then incubated with gentamicin (200 µg/ml) for 90 min after PBS was to kill extracellular bacteria. After incubation time cells were washed with PBS and subsequently lysed in 1% Triton-X 100, lysates were serially diluted and plated on LB agar plates. Bacteria colonies (CFU) were counted after overnight (16 h) incubation at 37 °C. To test effect of MDP, cells were pre-treated overnight with MDP (10 µg/ml).

Cytokine Assays

Cytokines including TNFA, IL6, IL1B and IL10 were measured in cell supernatant using ELISA MAX Deluxe kits from Biolegend as per manufacturer's protocol.

Statistics and reproducibility

All experimental values are presented as the means of replicate experiments ±SEM. Statistical analyses were performed using Prism 9 (GraphPad Software). Differences between the two groups were evaluated using Student's t-test (parametric) or Mann-Whitney U-test (non-parametric). To compare more than three groups, one-way analysis of variance followed by Tukey's post-hoc test was used. Differences at $P < 0.05$ were considered significant.

Acknowledgments

This work was supported by the National Institutes of Health (NIH) grant R01-AI141630 (to PG). PG and DS were also supported by the Leona M. and Harry B. Helmsley Charitable Trust and the NIH (UG3TR003355, UG3TR002968 and R01-AI55696). G.D.K. was supported through The American Association of Immunologists Intersect Fellowship Program for Computational Scientists and Immunologists, and American Heart Association's CDA award (24CDA1268506) S.S. was supported through The American Association of Immunologists Intersect Fellowship Program for Computational Scientists and Immunologists. Other sources of support include-- T32GM8806 (to D.V.). S-RI was supported by the postdoctoral fellowship grant from NIH (3R01DK107585-02S1). We thank Ying Jones (UC San Diego Electron Microscopy Core Facility) for technical and logistical support. This manuscript includes data generated at the UC San Diego Institute of Genomic Medicine (IGM) using an Illumina NovaSeq 6000 that was purchased with funding from a National Institutes of Health SIG grant (#S10 OD026929). The content is solely the responsibility of the authors and does not necessarily represent the official views of the Helmsley Charitable Trust or the National Institutes of Health.

Author contributions

G.D.K, M.A and P. G. conceptualized the project. G.D.K., M.A., S.S, J.C, Y.M, C.R.E, M.M and V.C, were involved in data curation and formal analysis. D.T.V, with supervision from D.S, carried out 16S microbiome analysis. S.S, with supervision from P.G carried out all the transcriptomic and proteomic analyses. G.D.K conducted all animal studies. M.A conducted all biochemical studies. V.C assisted G.D.K. for ELISA. Y.M assisted G.D.K. for qPCR and image analyses. C.R.E and S-R.I assisted M.A in construct design, cloning and mutagenesis. G.D.K. and P.G. prepared figures for data visualization, wrote the original draft, reviewed and edited the manuscript. P.G. supervised and acquired funding to support the study. All co-authors approved the final version of the manuscript.

FIGURES AND LEGENDS

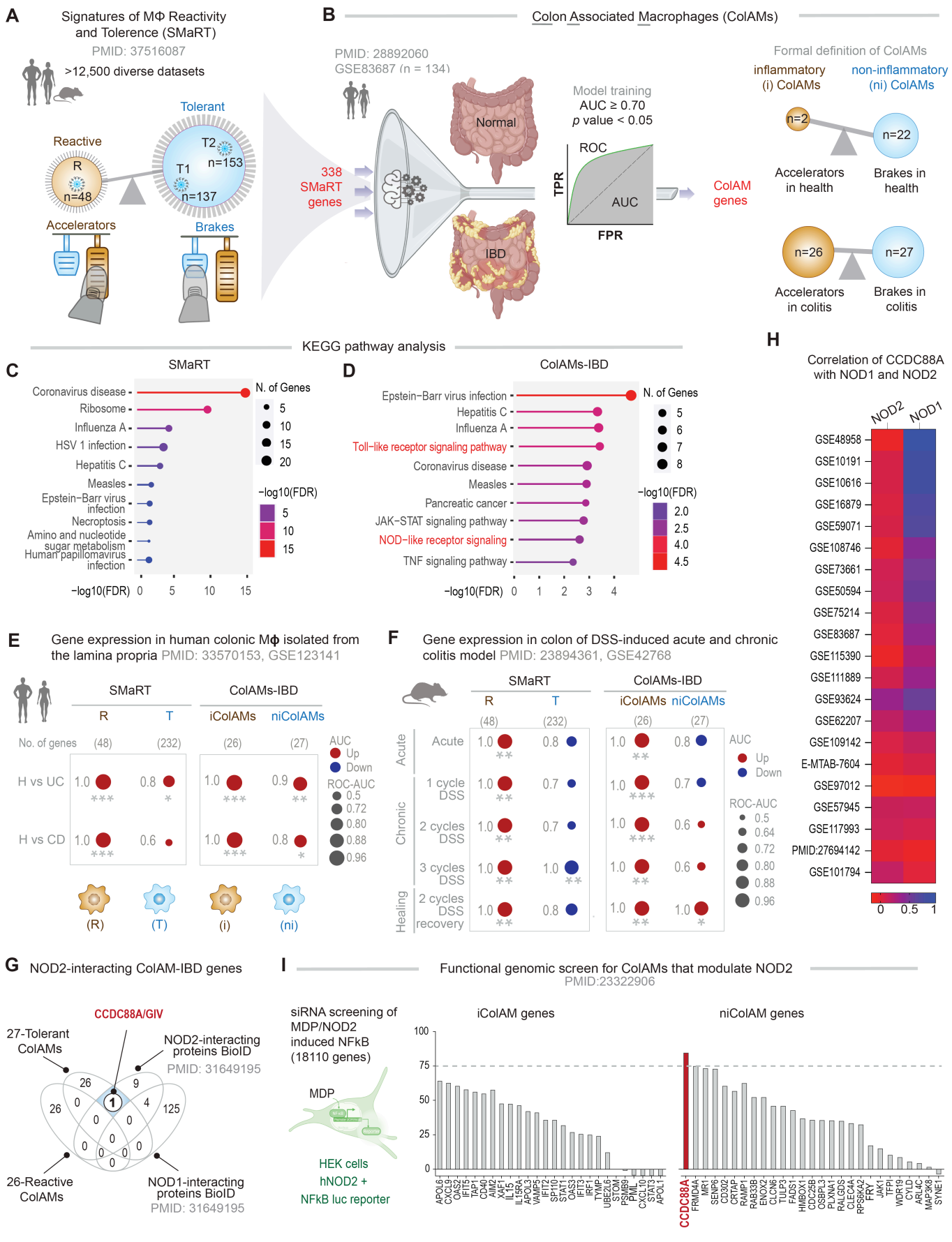

Figure 1. Identification of *CCDC88A* as a putative modulator of NOD2 in non-inflammatory ColAMΦs in IBD.

A. Key steps of the workflow used previously (3) to identify a computational model of macrophage continuum states, **S**ignatures of **M**acrophage **R**eactivity and **T**olerance (SMaRT) that charts invariant features of macrophage reactivity (R) and tolerance (T1 and T2) as interconnected gene clusters, identified using over 12,500 diverse transcriptomics datasets.

B. *Left*: Key steps used here to refine SMaRT in the context of the gut mucosa and derive colon-associated macrophage signatures (ColAMs) using a dataset (GSE83687) (13) comprised of both healthy and IBD samples. SMaRT genes were trained to derive a subset of ColAMs that could classify healthy vs IBD sample, achieving an area under the curve ≥ 0.7. *Right*: Inflammatory and non-inflammatory ColAMs identified here, in health (top) and IBD (bottom).

C-D. KEGG pathway enrichment analysis on the SMaRT (**C**) and the ColAM-IBD (**D**) genes.

E-F. Bubble plot displays ROC-AUC values (circle radii proportional to ROC-AUC) illustrating gene regulation directions (Up-regulated in red, Down-regulated in blue) for classifying healthy vs. CD and healthy vs. UC in human colonic lamina propria (GSE123141) (**E**) and DSS-induced acute, chronic and healing phase of murine colitis models (**F**). This classification is based on macrophage gene signatures of reactivity 'R' and tolerance 'T', identified in the SMaRT model and the i/niColAMs, used independently. Welch's two-sample unpaired t-test is applied to the composite gene signature score (z-score of normalized transcripts per million [tpm] count) to compute p-values (* $p \leq 0.05$; ** $p \leq 0.01$; *** $p \leq 0.001$).

G. Venn diagram shows the number of genes/proteins, identified by independent studies, to interact with NOD1/2. One gene/protein (CCDC88A/Girdin; white circle) interacts with NOD2 but not NOD1, is associated with tolerant ColAMs.

H. Heatmap of the correlation coefficient of normalized gene expression of *CCDC88A* with NOD1 and NOD2 in various independent datasets of healthy and IBD samples.

I. Bar graph shows siRNA screening of MDP/NOD2-induced NFκB activation in iColAMs (*left*) and niColAMs (*right*).

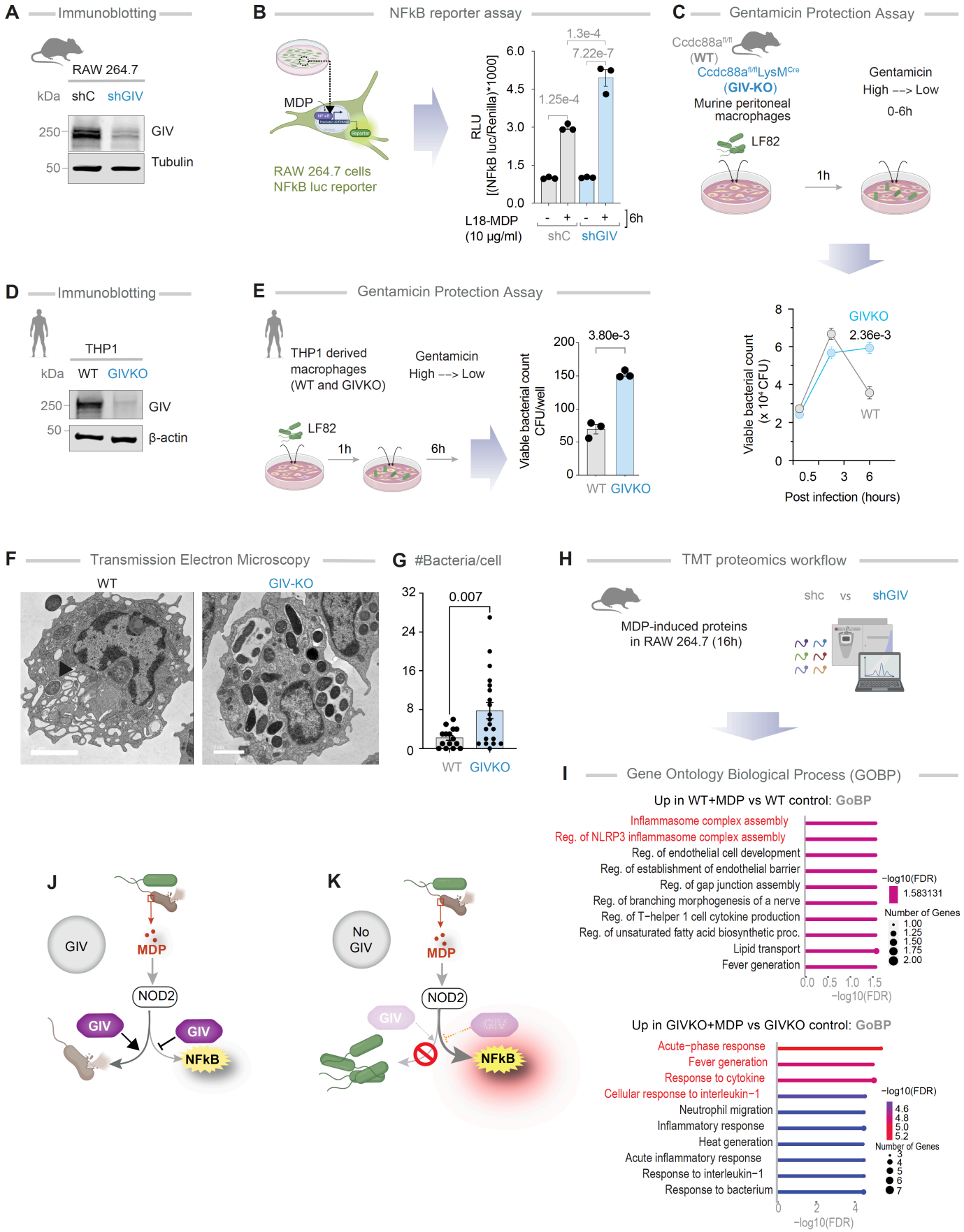

Figure 2. GIV is required for dampening MDP-stimulated inflammation and promoting bacterial clearance in macrophage.

A. Immunoblot of control (shC) or GIV-depleted (shGIV) RAW 264.7 cells.

B. Workflow of the NFκB reporter assay in RAW 264.7 cells (*left*). Bar graphs display the fold change in NFκB activity (*right*).

C. Schematic (top) displays the workflow for bacterial clearance assay. Line graphs (below) show the viable bacterial counts in the peritoneal macrophages.

D. Immunoblot of control (WT) or GIV-knockout (GIV-KO) THP1 monocyte derived macrophage.

E. Workflow of the gentamicin protection assay in THP1 cells. Bar graphs show the viable bacterial counts in the THP1 monocyte derived macrophage.

F-G. TEM micrographs (F) display representative fields of TG-PMs challenged with live AIEC-LF82 (MOI 1:30) for 1 h. Scale bar = 2 μM. Bar graphs (G) display findings based on ~20-30 randomly imaged fields; n = 2 repeats.

H-I: Workflow for multiplexed proteomics analyses (H). Bar graphs showing biological process as determined by gene ontology biological process analysis (Red, pathways cited in text).

J-K. Schematic summarizing findings in cells with GIV (J) and without GIV (K).

Statistics: All results are displayed as mean ± SEM (n=2-3 biological replicates). Significance was tested using two-way/one-way ANOVA followed by Tukey's test for multiple comparisons. *p*-value ≤ 0.05 is considered as significant.

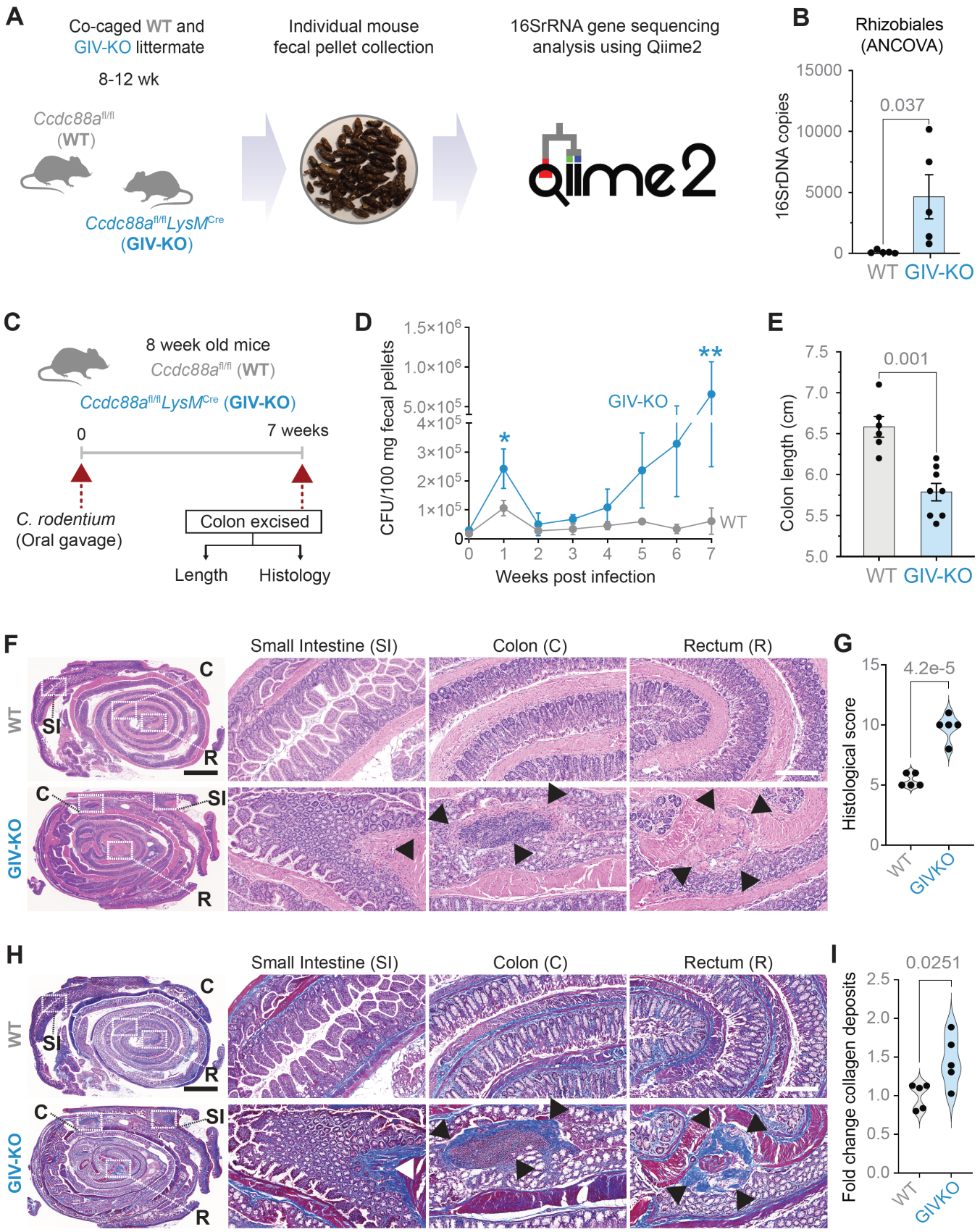

Figure 3. A mouse model of dysbiosis, impaired microbial clearance, patchy chronic transmural ileocolitis and fibrosis.

A-B. Schematic (A) and bar graph (B) display the process and outcome of a 16S fecal microbiome analysis at baseline in 10 wk-old myeloid-specific (*LysM*Cre) GIV-KO mice and their control littermates (WT). *p* value was estimated by unpaired t-test; n = 5 mice in each group.

C-I. Panels describing the experimental design (**C**) and findings (**D-I**) in an infectious colitis model of GIV-KO and control littermates induced using *Citrobacter rodentium* (initially termed *Citrobacter freundii* biotype 4280 (103); strain name DBS100; 5 x 10^8 CFU/200ul/mouse. GIV-KO, n=8; WT, n=6. Findings are representative of two independent repeats. Line graphs (**D**) display the bacterial burden in fecal pellets over a 7 wk period after the initial oral gavage. P values were determined by unpaired t-test. *, < 0.05; **, 0.01. Bar graph (**E**) displays the differences in colon length. *p* values were determined by unpaired t-test. H&E (**F**) or trichrome (**H**)-stained images representative of Swiss rolls of the entire intestinal tract are shown. Scale bar = 2.5 mm. Magnified fields of the rectum (R), colon (C) and small intestine (SI) (on the right) of the corresponding boxed regions (on the left) are shown. Scale bar = 250 μm. Arrows show regions of transmural inflammation/crypt distortion, immune infiltrates (in F) correspond also to transmural fibrosis (in H). Segments in between these patches appear normal. **(G)** Bar graphs show the histology index (104) (based on submucosal inflammation, percent area involved, inflammatory infiltrates in LP and crypt hyperplasia and the degree of fibrosis (**I**), as assessed by H&E and trichrome staining on n = 5 WT and 5 GIV-KO mice.

Statistics: *p* values were determined by unpaired t-test. All results are displayed as mean ± SEM.

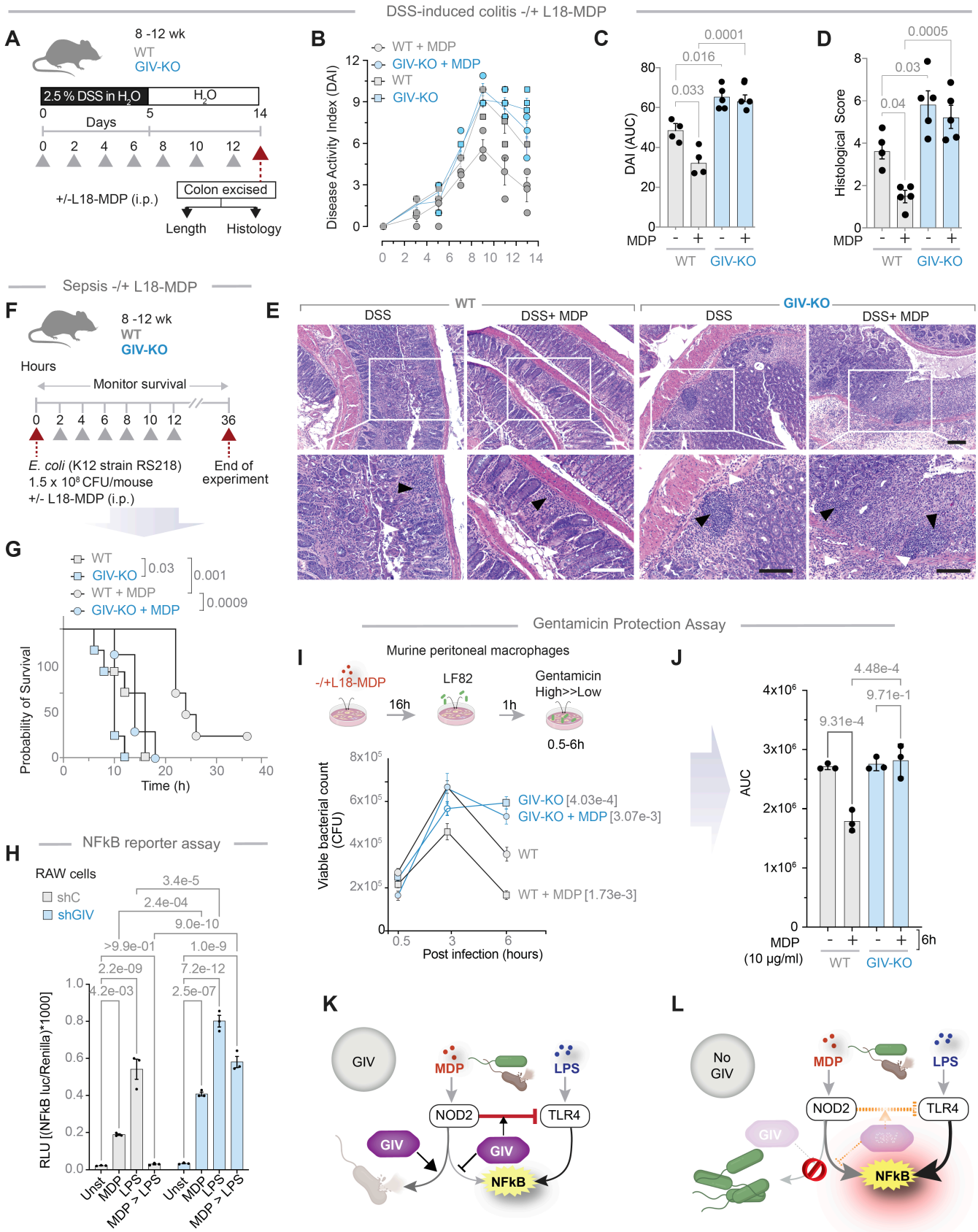

Figure 4. GIV-KO mice and cells are insensitive to the protective actions of MDP/NOD2 signals. A-E. Schematic (**A**) displays the study design for DSS-induced colitis. GIV-KO, n=5; WT, n=5. Findings are representative of two independent repeats. Grey arrowheads denote the alternate day administration of muramyl dipeptide (MDP) (100µg/mouse/day).

B-C. Line graphs (**B**) display disease activity index (DAI), calculated for the days 3, 5, 7, 9, 11 and 13 after DSS administration, which accounts for stool consistency (0-4), rectal bleeding (0-4), and weight loss (0-4). Bar graphs (**C**) represent the data in B as area under the curve (AUC). Bar graphs (**D**) display the histological score, as assessed by a well-accepted methodology (96) of analyzing H&E-stained distal colons from the mice. Representative images are displayed in **E**. Arrowheads point to regions of crypt destruction and/or inflammatory infiltrates. Scale bar = 200 μm.

F-G. Schematic (A) displays the sepsis study design in which 8 mice in each group were treated with E coli and MDP simultaneously, followed by periodic checks for death (arrowheads). Kaplan-Meier plot (B) displays the % of cohort that survived at those time points. GIV-KO, n=8; WT, n=8. Findings are representative of two independent repeats. *p* values were determined by Mantel-Cox log rank test. *p*-value ≤ 0.05 is considered as significant. All results are displayed as mean ± SEM.

H. Bar graphs display percent suppression of LPS-induced NFκB activity with MDP priming.

I-J. Schematic (top) displays the experimental set for bacterial clearance. Line graphs (below) show the viable bacterial counts in the macrophages. Bar graphs (**J**) represent the data in (**I)** as area under the curve (AUC).

K-L. Schematic summarizing findings in cells with (left, **K**) or without (right, **L**) GIV.

Statistics: All results are displayed as mean ± SEM (n=3 biological replicates). Significance was tested using two-way/one-way ANOVA followed by Tukey's test for multiple comparisons. *p*-value ≤ 0.05 is considered as significant.

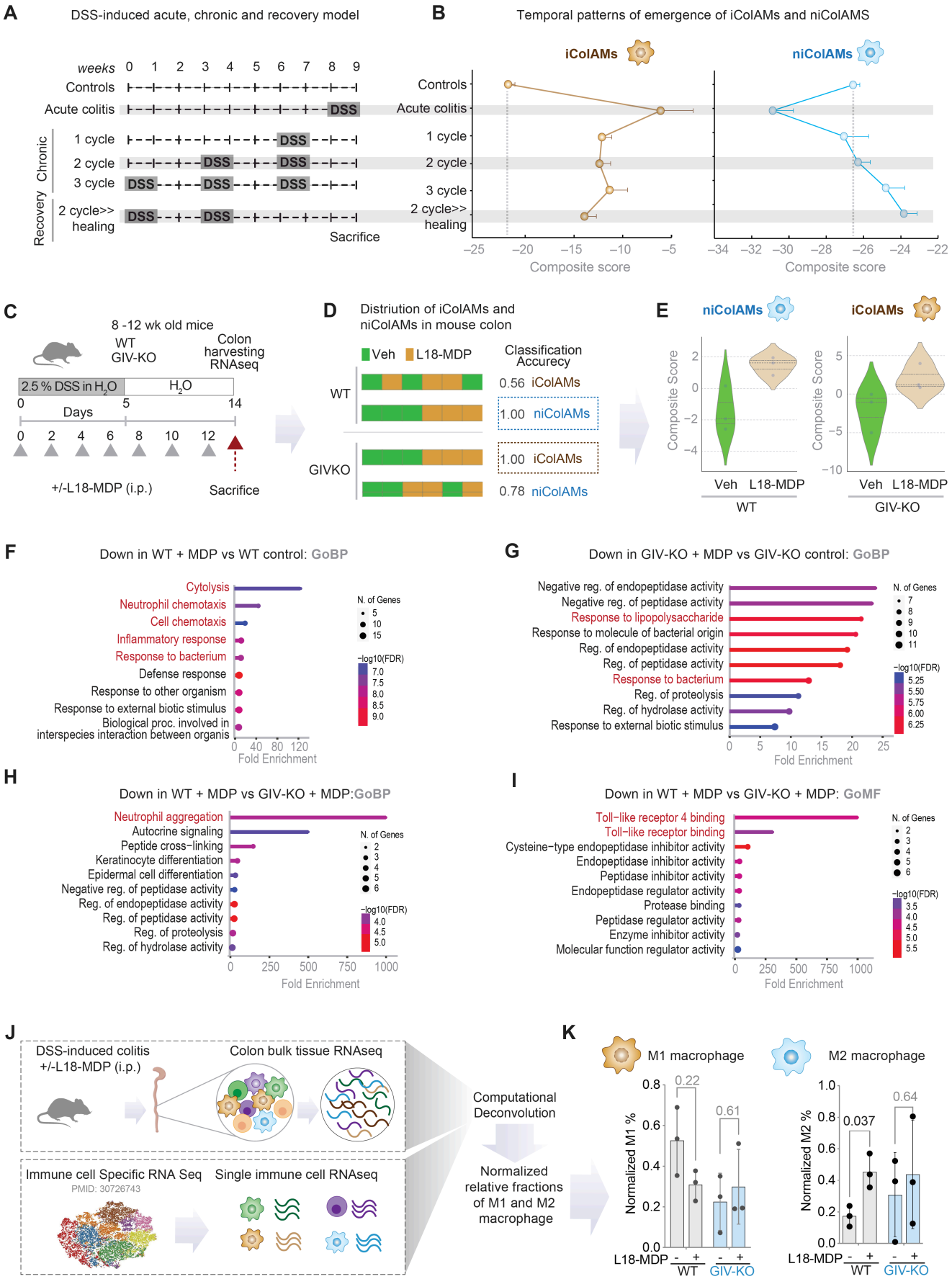

Figure 5. GIV is required for the emergence of healing niColAMs in MDP-.

A. Study design of DSS-induced acute, chronic and recovery in mouse models of colitis (C57/BL6; all WT).

B. Line graphs display the temporal patterns of the emergence of iColAMs and niColAMs in the colon samples in A.

C-E. Study design for DSS-induced colitis in WT vs. GIV mice (n=5 each). Grey arrowheads denote the alternate day administration of MDP (100 µg/mouse/day) (**C**). Bar plots (**D**) show the distribution patterns of iColAMs and niColAMs in the DSS *vs*. DSS+MDP samples. Classification strength within each cohort is measured using ROC-AUC analyses. Violin plots (**E**) show composite scores for niColAMs (left, blue border) in WT and iColAMs (right, brown border) in GIV-KO mice, treated with or without MDP.

F-G. Gene Ontology Biological Process (Go-BP) pathway enrichment analyses of genes downregulated in WT (F) or GIV-KO (G) mice treated with L18-MDP compared to their respective untreated controls.

H-I. GoBP (H) and Go Molecular Function (GoMF; I) analyses of genes downregulated in L18-MDP-treated WT vs. GIV-KO samples.

J-K. Schematic (J) of bulk RNA sequencing (Bulk Seq) *in silico* deconvolution analysis of distal colons from DSS-treated mice in C. Bar plots (K) show normalized percentage abundances of M1 and M2 macrophages in WT and GIV-KO mice, with and without MDP treatment.

Statistics: *p* values were calculated using one-way ANOVA, followed by Tukey's test for multiple comparisons and indicated with *p*-values shown above bars. *p*-value ≤ 0.05 is considered as significant.

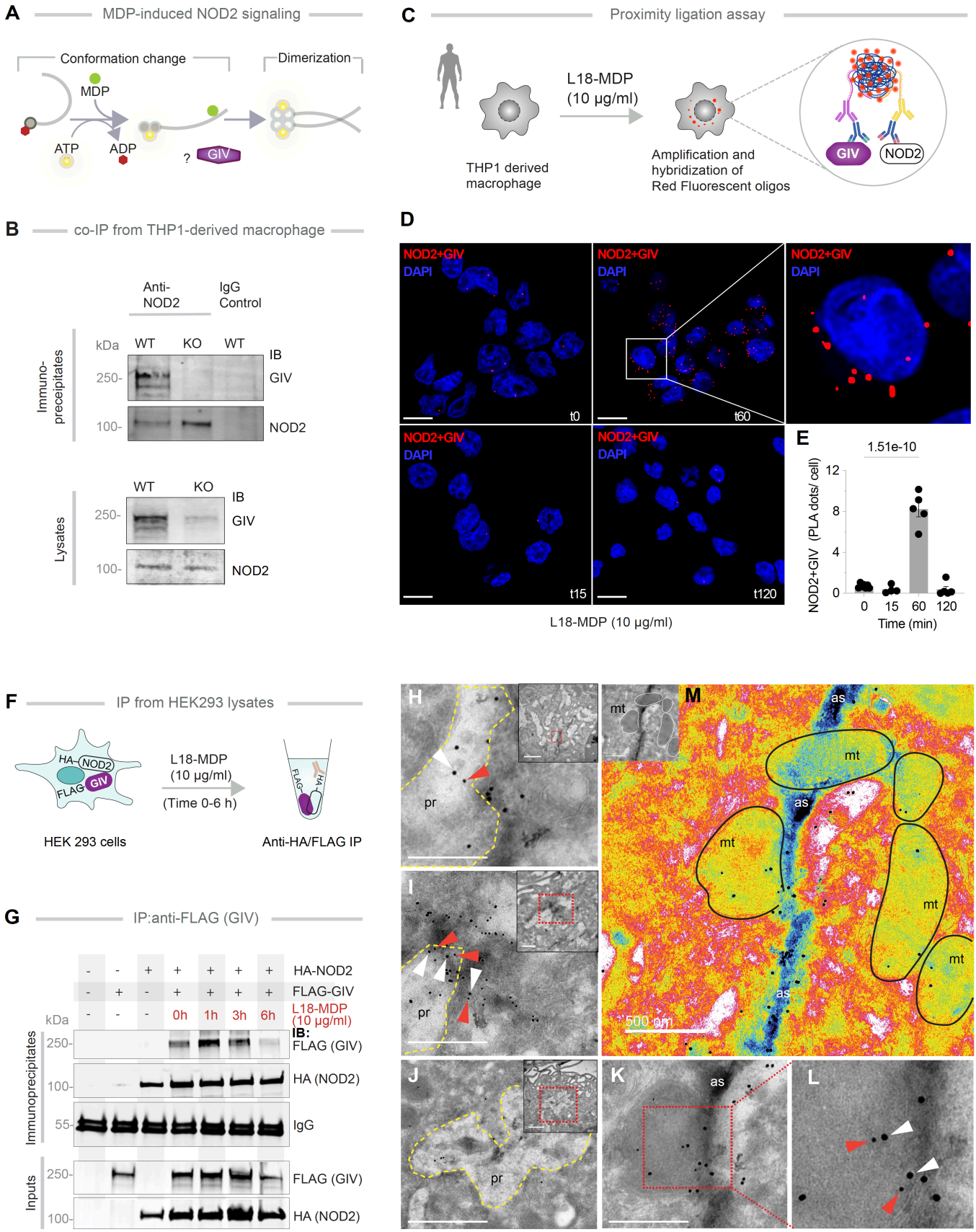

Figure 6. NOD2 and GIV colocalize and interact in cells

A. Schematic displays key steps in MDP-induced NOD2 signaling. In resting cells, ADP-bound inactive NOD2 exists in an autoinhibited conformation. Upon ligand (MDP) stimulation, ADP is exchanged for ATP, which

further enhances MDP (ligand) binding-associated with conformational change and 'opening' of the LRR module. Subsequently, NOD2 dimerizes and forms complexes with other signaling proteins.

B. Full length endogenous NOD2 was immunoprecipitated from THP1 derived macrophage lysates. Immune complexes were analyzed for bound GIV (top) and equal aliquots of lysates were analyzed for NOD2 and GIV (bottom) by immunoblotting (IB).

C-E. Study design of PLA (**C**) and representative confocal images (**D**) display colocalization of GIV and NOD2 in THP1 derived macrophages challenged with MDP for 0-120 min. Scale bar = 10 µm. Bar graphs (**E**) display findings based on ~20-30 randomly imaged fields; n = 4-5 repeats. *p* value was calculated using one-way ANOVA, followed by Tukey's test for multiple comparisons and indicated with *p*-values shown above bars. *p*-value ≤ 0.05 is considered as significant.

F-G. Schematic depicts study design of immunoprecipitation (**F**). HA-tagged NOD2 was immunoprecipitated with anti-HA mAb from equal aliquots of lysates of HEK293T cells expressing GIV-FLAG and HA-NOD2, stimulated (+) or not (-) with MDP for indicated time points. Immunoprecipitated (IP; top) complexes and input (bottom) lysates were analyzed for NOD2 and GIV by immunoblotting (IB) (**G**).

H-M. TEM micrographs display representative images of colocalization of GIV (white arrowheads; 18 nm gold particles) and NOD2 (red arrowheads; 12 nm gold particles) on TG-PMs challenged with live AIEC-LF82 (MOI 1:30) for 1 h. NOD2 colocalization within particle-rich cytoplasmic structures (pr), with membrane-associated GIV on actin strands (as, Pseudo-colored blue) and swollen mitochondria (mt, outlined in black) with degraded cristae in **M** and. Scale bar = 500 nM.

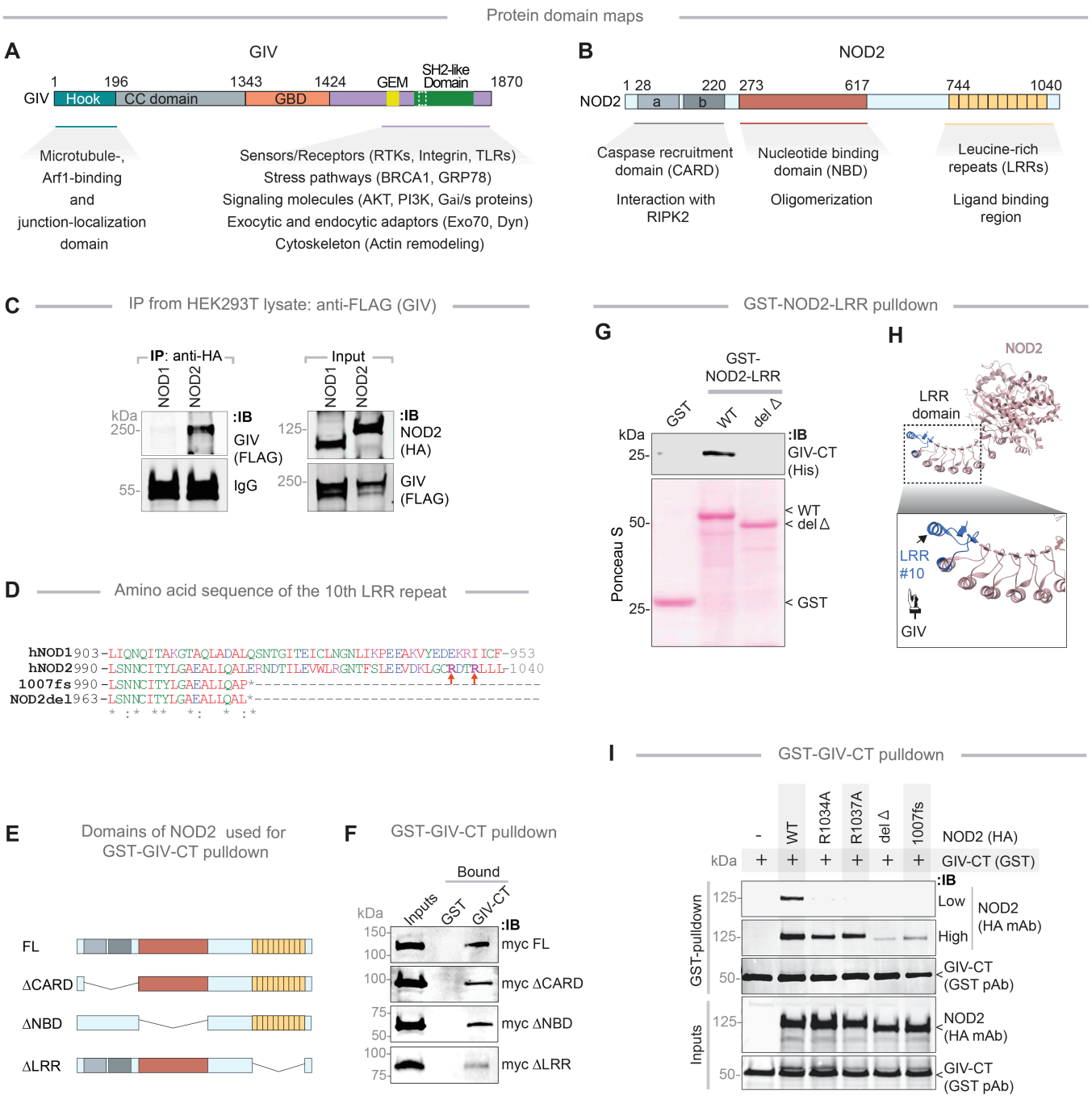

Figure 7. The NOD2(LRR)•GIV(C-term) interaction is direct and ligand-dependent

A-B. Schematic depicts the domain maps of (A) GIV and (B) NOD2.

C. HA-tagged NOD1/2 proteins were immunoprecipitated from equal aliquots of lysates of HEK293T cells co-transfected with GIV and either NOD1 or NOD2 using anti-HA mAb. Immunoprecipitated (IP; left) complexes and input (right) lysates were analyzed for NOD1/2 and GIV by immunoblotting (IB).

D. An alignment of the amino acid sequence of the 10th LRR repeat of human hNOD1, hNOD2, the CD-risk associated NOD2 variant (NOD2-*1007fs*) and the deletion mutant generated in this work (NOD2-del) is shown. Residues mutated in this study to evaluate potential participating residues in the NOD2•GIV interaction are highlighted.

E-F. Schematics indicate the domains of NOD2 that were used to generate myc-tagged recombinant proteins for use in GST-pulldown assays in **E**. Equal aliquots of recombinant myc-NOD2 domains (~3 μg; input, **F**) were used in pulldown assays with immobilized GST and GST-GIV in **F**. Myc-tagged NOD2 was visualized by immunoblot (IB) using anti-myc antibody.

G-H. GST-pulldown assay (G) was carried out using GST NOD2-LRR proteins as indicated and bound His-GIV-CT is assessed. Schematic (H) highlights the terminal LRR repeat (blue) of NOD2 which binds GIV.

I. GST-GIV-CT was pulled down using Glutathione beads from equal aliquots of lysates of HEK293T lysates co-expressing GST-GIV-CT (aa 1660-1870; mammalian p-CEFL vector) and either WT or HA-NOD2 mutants predicted to disrupt NOD•GIV binding. Immunoprecipitated (IP; top) complexes and input (bottom) lysates were analyzed for NOD2 and GIV-CT by immunoblotting (IB), using anti-HA (NOD2) and anti-GST (GIV-CT) antibodies.

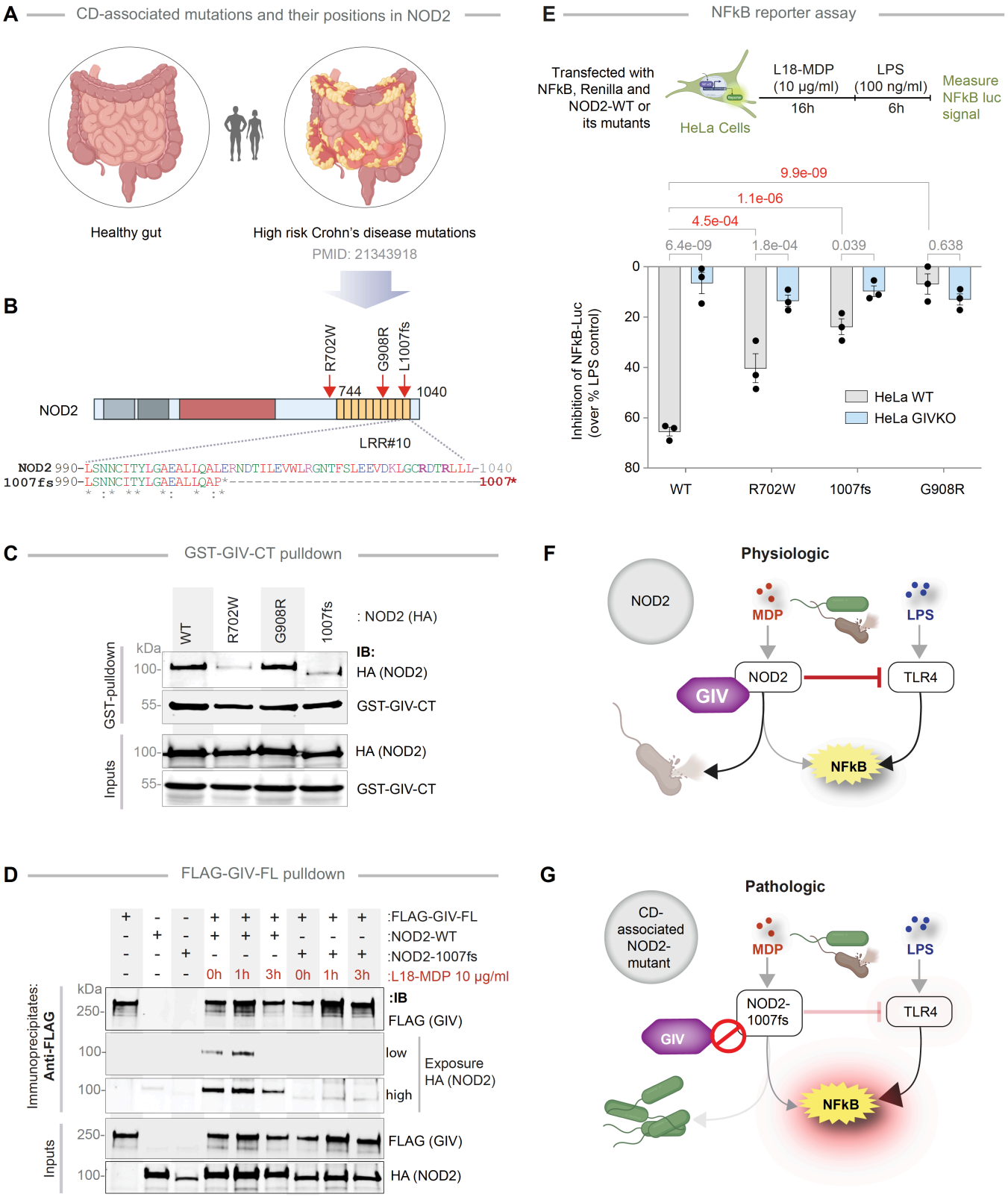

Figure 8: Characterization of the NOD2•GIV interface exploiting CD associated NOD2 mutants.

A-B. Schematic shows (A) CD-associated mutations and their positions in NOD2, depicts as a domain map (B). *Bottom*: An alignment of the amino acid sequence of the 10th LRR repeat of human NOD2 and the CD-risk associated NOD2 variant (NOD2-*1007fs*) are shown. Residues mutated in this study to evaluate potential participating residues in the NOD2•GIV interaction are highlighted.

C. GST-GIV-CT was pulled down using Glutathione beads from equal aliquots of lysates of HEK293T lysates co-expressing GST-GIV-CT (aa 1660-1870; mammalian p-CEFL vector) and wild-type (WT) or 3 indicated CD-risk associated variants of HA-NOD2. Bound NOD2 proteins and similar expression of GIV-CT was assessed by immunoblotting (IB) using anti-HA (NOD2) and anti-GST (GIV-CT) antibodies.

D. FLAG-tagged GIV was immunoprecipitated with anti-FLAG mAb from equal aliquots of lysates of HEK293T cells expressing GIV-FLAG and either wild-type (WT) or *1007fs* variant of HA-NOD2, stimulated (+) or not (-) with MDP for indicated time points. Immunoprecipitated (IP; top) complexes and input (bottom) lysates were analyzed for NOD2 and GIV by immunoblotting (IB), using anti-HA (NOD2) and anti-FLAG (GIV-CT) antibodies.

E. Bar graphs display NFκB reporter assay in HeLa cells. Cells were pre-incubated with MDP (1 μg/ml) and then stimulated with LPS (100 ng/ml) and % change of NFκB activity was detected using dual cell reporter assay.

F-G. Schematic summarizing key findings in this work. Magenta colored solid and interrupted lines indicate the GIV-dependent impact on NOD2 that were interrogated in this work. (**F**) *Top*: In physiology, bacterial sensing and signaling by NOD2 requires GIV to limit inflammation. (**G**) In pathology, dysregulated inflammation results when either wild-type NOD2 cannot bind GIV (e.g., GIV is low/absent) or when CD-risk associated *1007fs* variant cannot bind GIV.

Statistics: *p* values were calculated using two-way ANOVA and indicated with *p*-values shown above bars. *p*-value ≤ 0.05 is considered as significant.

TABLES

Table 1: List of reagents and resources

REAGENT or RESOURCE	SOURCE	IDENTIFIER
Biological Samples and Cell Lines		
Adherent-invasive *E. coli* LF82 (AIEC-LF82)	Prof. Arlette Darfeuille-Michaud	(47)
***E. coli* (strain RS218)**	Prof. Victor Nizet	(44)
Citrobacter rodentium (strain DBS100)	ATCC (105)	
RAW 264.7	ATCC	TIB-71
shControl RAW 264.7	(44)	
shGIV RAW 264.7	(44)	
HEK293T	ATCC	ATCC® CRL-11268
HeLa parental	ATCC	ATCC® CCL-2
HeLa GIV KO (CRISPR Cas9)	(106)	n/a
LysMcre mice (B6.129P2-Lyz2$^{tm1(cre)Ifo}$/j)	The Jackson Laboratory	004781
Girdin flox mice	Asai et al. Biochem. Biophys. Res. Commun., 2012	N/A
Ccdc88a$^{fl/fl}$ LysM$^{Cre/-}$ mice	(44)	
Chemicals and Reagents		
L18-MDP	Invivogen	
Lipopolysaccharide (E. coli O111:B4)	Sigma-Aldrich	L4391
PowerUpä SYBR^{ä} Green Master Mix	Applied Biosciences	A25741
qScript^{ä} cDNA SuperMix	QuantaBio	101414
Direct-zol RNA Miniprep Kit	Zymo Research	R1051
TRIzol^{ä} Reagent	Invitrogen	15596018
ELISA MAX^{ä} Deluxe Set Mouse IL-6	BioLegend	431304
ELISA MAX^{ä} Deluxe Set Mouse IL-1b	BioLegend	432604
ELISA MAX^{ä} Deluxe Set Mouse IL-10	BioLegend	431414
ELISA MAX^{ä} Deluxe Set Mouse TNF-a	BioLegend	
Dextran Sulfate Sodium Salt (Colitis Grade)	MP Biomedicals, LLC	160110
Hemoccult II	Beckman Coulter	61130
Zinc Formalin Fixative	Sigma-Aldrich	Z2902
Primers		
Species/Targets	Forward primer (5'→ 3')	Reverse primer (3'→ 5')
Mouse IL-6 qPCR primers	TGGAGTCACAGAAGGAGTGGCTAAG	TCTGACCACAGTGAGGAATGTCCAC
Mouse IL-1b qPCR primers	GCCTTGGGCCTCAAAGGAAAGAATC	GGAAGACACAGATTCCATGGTGAAG
Mouse TNFA qPCR primers	ATAGCTCCCAGAAAAGCAAGC	CACCCCGAAGTTCAGTAGACA
Mouse IL-10 qPCR primers	CCCTGGGTGAGAAGCTGAAG	CACTGCCTTGCTCTTATTTTCACA
Mouse 18S qPCR primers	GTAACCCGTTGAACCCCATT	CCATCCAATCGGTAGTAGCG
V4 region of the 16S rRNA gene	GTGYCAGCMGCCGCGGTAA (515F, Parada)	GGACTACNVGGGTWTCTAAT (806R, Apprill)
Software		
ImageJ	National Institute of Health	https://imagej.net/Welcome

Prism 9	GraphPad	https://www.graphpad.com/scientific-software/prism/
Molsoft	Molsoft, LLC	https://www.molsoft.com/index.html
LAS-X	Leica	www.leica-microsystems.com/products/microscope-software/p/leica-las-x-ls
SnapGene	GSL Biotech LLC	https://www.snapgene.com/
Illustrator	Adobe	https://www.adobe.com/products/illustrator.html
ImageStudio Lite	LI-COR	https://www.licor.com/bio/image-studio-lite/
ClueGO	Cytoscape	https://academic.oup.com/bioinformatics/article/25/8/1091/324247
NetworkX	Python	https://networkx.org
Gephi	Gephi	https://gephi.org
Plasmid		
pET-28b-GIV-CT-WT (aa 1660-1870)	(107)	Referred to as His-GIV-CT (aa 1660-1870)
pGEX-4T-GIV-CT-WT (a.a. 1623-1870)	(107)	Referred to as GST-GIV-CT (aa 1660-1870)
pCEFL-GST-GIV-CT (1660-1870)	(108)	Referred to as pCEFL GST-GIV-CT for mammalian expression (aa 1660-1870)
CMV14-p3X FLAG-GIV WT (full length)	(107)	N/A
pcDNA5-FRT-TO-RIP2-WT	(62)	Addgene 131201
HA-tagged NOD2-WT	From Dana J. Philpott (University of Toronto, Canada); originally from M. D'Amato (Karolinska Institute) (97)	N/A
HA-tagged NOD1		
HA-tagged NOD2-1007fs	*This paper*	
HA-tagged NOD2-G908R		
HA-tagged NOD2-R702W		
HA-tagged NOD2-R1034A		
HA-tagged NOD2-R1037A		
HA-tagged NOD2-LRR- delΔ		
pCMV-Myc-tagged NOD2-FL-WT (Cloning site: XhoI/NotI)		
pGEX-6P-2-NOD2-LRR (aa 744-1040) (Cloning site: BamHI/XhoI)		aa numbering according to Protein hNOD2 : UniProtKB/Swiss-Prot: Q9HC29.1
pGEX-6P-2-NOD2-LRR-R1034A LRR (aa 744-1040)		
pGEX-6P-2-NOD2-LRR-R1037A LRR (aa 744-1040)		
pGEX-6P-2-NOD2-LRR- delΔ (aa 744-1006)		

REFERENCES

1. Yang W, and Cong Y. Gut microbiota-derived metabolites in the regulation of host immune responses and immune-related inflammatory diseases. *Cell Mol Immunol.* 2021;18(4):866-77.
2. Katkar G, and Ghosh P. Macrophage states: there's a method in the madness. *Trends Immunol.* 2023;44(12):954-64.
3. Ghosh P, Sinha S, Katkar GD, Vo D, Taheri S, Dang D, et al. Machine learning identifies signatures of macrophage reactivity and tolerance that predict disease outcomes. *EBioMedicine.* 2023;94:104719.
4. Marks DJ. Defective innate immunity in inflammatory bowel disease: a Crohn's disease exclusivity? *Curr Opin Gastroenterol.* 2011;27(4):328-34.
5. Davies JM, and Abreu MT. The innate immune system and inflammatory bowel disease. *Scand J Gastroenterol.* 2015;50(1):24-33.
6. Gordon S, and Plüddemann A. Tissue macrophages: heterogeneity and functions. *BMC Biol.* 2017;15(1):53.
7. Sahoo D, Swanson L, Sayed IM, Katkar GD, Ibeawuchi SR, Mittal Y, et al. Artificial intelligence guided discovery of a barrier-protective therapy in inflammatory bowel disease. *Nat Commun.* 2021;12(1):4246.
8. Sahoo D, Katkar GD, Khandelwal S, Behroozikhah M, Claire A, Castillo V, et al. AI-guided discovery of the invariant host response to viral pandemics. *EBioMedicine.* 2021;68:103390.
9. Pandya R, He YD, Sweeney TE, Hasin-Brumshtein Y, and Khatri P. A machine learning classifier using 33 host immune response mRNAs accurately distinguishes viral and non-viral acute respiratory illnesses in nasal swab samples. *Genome Med.* 2023;15(1):64.
10. Zhang Z, Tao W, Cheng D, Qin M, Fu J, and Liu D. Deciphering the crosstalk of immune dysregulation between COVID-19 and idiopathic inflammatory myopathy. *Front Immunol.* 2023;14:1197493.
11. Dalerba P, Sahoo D, Paik S, Guo X, Yothers G, Song N, et al. CDX2 as a Prognostic Biomarker in Stage II and Stage III Colon Cancer. *N Engl J Med.* 2016;374(3):211-22.
12. Ghosh P, Campos VJ, Vo DT, Guccione C, Goheen-Holland V, Tindle C, et al. AI-assisted discovery of an ethnicity-influenced driver of cell transformation in esophageal and gastroesophageal junction adenocarcinomas. *JCI Insight.* 2022;7(18).
13. Peters LA, Perrigoue J, Mortha A, Iuga A, Song WM, Neiman EM, et al. A functional genomics predictive network model identifies regulators of inflammatory bowel disease. *Nat Genet.* 2017;49(10):1437-49.
14. Breynaert C, Dresselaers T, Perrier C, Arijs I, Cremer J, Van Lommel L, et al. Unique gene expression and MR T2 relaxometry patterns define chronic murine dextran sodium sulphate colitis as a model for connective tissue changes in human Crohn's disease. *PLoS One.* 2013;8(7):e68876.
15. Jostins L, Ripke S, Weersma RK, Duerr RH, McGovern DP, Hui KY, et al. Host-microbe interactions have shaped the genetic architecture of inflammatory bowel disease. *Nature.* 2012;491(7422):119-24.
16. Liu JZ, van Sommeren S, Huang H, Ng SC, Alberts R, Takahashi A, et al. Association analyses identify 38 susceptibility loci for inflammatory bowel disease and highlight shared genetic risk across populations. *Nat Genet.* 2015;47(9):979-86.
17. Philpott DJ, Sorbara MT, Robertson SJ, Croitoru K, and Girardin SE. NOD proteins: regulators of inflammation in health and disease. *Nat Rev Immunol.* 2014;14(1):9-23.
18. Caruso R, Warner N, Inohara N, and Núñez G. NOD1 and NOD2: signaling, host defense, and inflammatory disease. *Immunity.* 2014;41(6):898-908.
19. McCarthy JV, Ni J, and Dixit VM. RIP2 is a novel NF-kappaB-activating and cell death-inducing kinase. *J Biol Chem.* 1998;273(27):16968-75.
20. Nachbur U, Stafford CA, Bankovacki A, Zhan Y, Lindqvist LM, Fiil BK, et al. A RIPK2 inhibitor delays NOD signalling events yet prevents inflammatory cytokine production. *Nat Commun.* 2015;6:6442.
21. Lesage S, Zouali H, Cézard JP, Colombel JF, Belaiche J, Almer S, et al. CARD15/NOD2 mutational analysis and genotype-phenotype correlation in 612 patients with inflammatory bowel disease. *Am J Hum Genet.* 2002;70(4):845-57.
22. Kufer TA, Banks DJ, and Philpott DJ. Innate immune sensing of microbes by Nod proteins. *Ann N Y Acad Sci.* 2006;1072:19-27.
23. Rescigno M, and Nieuwenhuis EE. The role of altered microbial signaling via mutant NODs in intestinal inflammation. *Curr Opin Gastroenterol.* 2007;23(1):21-6.

24. Vignal C, Singer E, Peyrin-Biroulet L, Desreumaux P, and Chamaillard M. How NOD2 mutations predispose to Crohn's disease? *Microbes Infect.* 2007;9(5):658-63.
25. Nelson A, Stewart CJ, Kennedy NA, Lodge JK, Tremelling M, Probert CS, et al. The Impact of NOD2 Genetic Variants on the Gut Mycobiota in Crohn's Disease Patients in Remission and in Individuals Without Gastrointestinal Inflammation. *J Crohns Colitis.* 2021;15(5):800-12.
26. Lu Y, Zheng Y, Coyaud É, Zhang C, Selvabaskaran A, Yu Y, et al. Palmitoylation of NOD1 and NOD2 is required for bacterial sensing. *Science.* 2019;366(6464):460-7.
27. Warner N, Burberry A, Franchi L, Kim YG, McDonald C, Sartor MA, et al. A genome-wide siRNA screen reveals positive and negative regulators of the NOD2 and NF-κB signaling pathways. *Sci Signal.* 2013;6(258):rs3.
28. Ashton JJ, Boukas K, Stafford IS, Cheng G, Haggarty R, Coelho TAF, et al. Deleterious Genetic Variation Across the NOD Signaling Pathway Is Associated With Reduced NFKB Signaling Transcription and Upregulation of Alternative Inflammatory Transcripts in Pediatric Inflammatory Bowel Disease. *Inflamm Bowel Dis.* 2022.
29. Graham DB, and Xavier RJ. Pathway paradigms revealed from the genetics of inflammatory bowel disease. *Nature.* 2020;578(7796):527-39.
30. Hugot JP, Chamaillard M, Zouali H, Lesage S, Cézard JP, Belaiche J, et al. Association of NOD2 leucine-rich repeat variants with susceptibility to Crohn's disease. *Nature.* 2001;411(6837):599-603.
31. Ogura Y, Bonen DK, Inohara N, Nicolae DL, Chen FF, Ramos R, et al. A frameshift mutation in NOD2 associated with susceptibility to Crohn's disease. *Nature.* 2001;411(6837):603-6.
32. Eckmann L, and Karin M. NOD2 and Crohn's disease: loss or gain of function? *Immunity.* 2005;22(6):661-7.
33. Rogler G, Brand K, Vogl D, Page S, Hofmeister R, Andus T, et al. Nuclear factor kappaB is activated in macrophages and epithelial cells of inflamed intestinal mucosa. *Gastroenterology.* 1998;115(2):357-69.
34. Maeda S, Hsu LC, Liu H, Bankston LA, Iimura M, Kagnoff MF, et al. Nod2 mutation in Crohn's disease potentiates NF-kappaB activity and IL-1beta processing. *Science.* 2005;307(5710):734-8.
35. Economou M, Trikalinos TA, Loizou KT, Tsianos EV, and Ioannidis JP. Differential effects of NOD2 variants on Crohn's disease risk and phenotype in diverse populations: a metaanalysis. *Am J Gastroenterol.* 2004;99(12):2393-404.
36. Freire P, Cardoso R, Figueiredo P, Donato MM, Ferreira M, Mendes S, et al. NOD2 gene mutations in ulcerative colitis: useless or misunderstood? *Int J Colorectal Dis.* 2014;29(6):653-61.
37. Watanabe T, Kitani A, Murray PJ, and Strober W. NOD2 is a negative regulator of Toll-like receptor 2-mediated T helper type 1 responses. *Nat Immunol.* 2004;5(8):800-8.
38. Watanabe T, Asano N, Murray PJ, Ozato K, Tailor P, Fuss IJ, et al. Muramyl dipeptide activation of nucleotide-binding oligomerization domain 2 protects mice from experimental colitis. *J Clin Invest.* 2008;118(2):545-59.
39. Watanabe T, Kitani A, and Strober W. NOD2 regulation of Toll-like receptor responses and the pathogenesis of Crohn's disease. *Gut.* 2005;54(11):1515-8.
40. Watanabe T, Asano N, Meng G, Yamashita K, Arai Y, Sakurai T, et al. NOD2 downregulates colonic inflammation by IRF4-mediated inhibition of K63-linked polyubiquitination of RICK and TRAF6. *Mucosal Immunol.* 2014;7(6):1312-25.
41. Negroni A, Pierdomenico M, Cucchiara S, and Stronati L. NOD2 and inflammation: current insights. *J Inflamm Res.* 2018;11:49-60.
42. Ghosh P, Rangamani P, and Kufareva I. The GAPs, GEFs, GDIs and...now, GEMs: New kids on the heterotrimeric G protein signaling block. *Cell Cycle.* 2017;16(7):607-12.
43. Ghosh P, and Mullick M. Building unconventional G protein-coupled receptors, one block at a time. *Trends Pharmacol Sci.* 2021;42(7):514-7.
44. Swanson L, Katkar GD, Tam J, Pranadinata RF, Chareddy Y, Coates J, et al. TLR4 signaling and macrophage inflammatory responses are dampened by GIV/Girdin. *Proc Natl Acad Sci U S A.* 2020;117(43):26895-906.
45. Damgaard RB, Nachbur U, Yabal M, Wong WW, Fiil BK, Kastirr M, et al. The ubiquitin ligase XIAP recruits LUBAC for NOD2 signaling in inflammation and innate immunity. *Mol Cell.* 2012;46(6):746-58.
46. Hao H, Xu F, Hao J, He YQ, Zhou XY, Dai H, et al. Lipoxin A4 suppresses lipopolysaccharide-induced hela cell proliferation and migration via NF-κB pathway. *Inflammation.* 2015;38(1):400-8.

47. Darfeuille-Michaud A, Boudeau J, Bulois P, Neut C, Glasser AL, Barnich N, et al. High prevalence of adherent-invasive Escherichia coli associated with ileal mucosa in Crohn's disease. *Gastroenterology.* 2004;127(2):412-21.
48. Kaakoush NO, Day AS, Huinao KD, Leach ST, Lemberg DA, Dowd SE, et al. Microbial dysbiosis in pediatric patients with Crohn's disease. *J Clin Microbiol.* 2012;50(10):3258-66.
49. Cobb JP, Brown CM, Brown GL, and Polk HC, Jr. Muramyl dipeptide protects decomplemented mice from surgically-induced infection. *Int J Immunopharmacol.* 1986;8(7):799-803.
50. Matsumoto K, Ogawa H, Nagase O, Kusama T, and Azuma I. Stimulation of nonspecific host resistance to infection induced by muramyldipeptides. *Microbiol Immunol.* 1981;25(10):1047-58.
51. Wardowska A, Dzierzbicka K, Szaryńska M, Dabrowska-Szponar M, Wiśniewska K, Myśliwski A, et al. Analogues of muramyl dipeptide (MDP) and tuftsin limit infection and inflammation in murine model of sepsis. *Vaccine.* 2009;27(3):369-74.
52. Katkar GD, Sayed IM, Anandachar MS, Castillo V, Vidales E, Toobian D, et al. Artificial Intelligence-rationalized balanced PPARα/γ dual agonism resets the dysregulated macrophage processes in inflammatory bowel disease. *bioRxiv.* 2021:2021.07.18.452807.
53. Whittem CG, Williams AD, and Williams CS. Murine Colitis modeling using Dextran Sulfate Sodium (DSS). *J Vis Exp.* 2010(35).
54. Kim H, Zhao Q, Zheng H, Li X, Zhang T, and Ma X. A novel crosstalk between TLR4- and NOD2-mediated signaling in the regulation of intestinal inflammation. *Sci Rep.* 2015;5:12018.
55. Wang J, Lin D, Peng H, Shao J, and Gu J. Cancer-derived immunoglobulin G promotes LPS-induced proinflammatory cytokine production via binding to TLR4 in cervical cancer cells. *Oncotarget.* 2014;5(20):9727-43.
56. Jiang N, Xie F, Guo Q, Li MQ, Xiao J, and Sui L. Toll-like receptor 4 promotes proliferation and apoptosis resistance in human papillomavirus-related cervical cancer cells through the Toll-like receptor 4/nuclear factor-κB pathway. *Tumour Biol.* 2017;39(6):1010428317710586.
57. Manna SK, and Aggarwal BB. Lipopolysaccharide inhibits TNF-induced apoptosis: role of nuclear factor-kappaB activation and reactive oxygen intermediates. *J Immunol.* 1999;162(3):1510-8.
58. Sulistyowati E, Lee MY, Wu LC, Hsu JH, Dai ZK, Wu BN, et al. Exogenous Heat Shock Cognate Protein 70 Suppresses LPS-Induced Inflammation by Down-Regulating NF-κB through MAPK and MMP-2/-9 Pathways in Macrophages. *Molecules.* 2018;23(9).
59. Xiong D, Song L, Geng S, Jiao Y, Zhou X, Song H, et al. Salmonella Coiled-Coil- and TIR-Containing TcpS Evades the Innate Immune System and Subdues Inflammation. *Cell Rep.* 2019;28(3):804-18.e7.
60. Pridmore AC, Jarvis GA, John CM, Jack DL, Dower SK, and Read RC. Activation of toll-like receptor 2 (TLR2) and TLR4/MD2 by Neisseria is independent of capsule and lipooligosaccharide (LOS) sialylation but varies widely among LOS from different strains. *Infect Immun.* 2003;71(7):3901-8.
61. Gong Q, Long Z, Zhong FL, Teo DET, Jin Y, Yin Z, et al. Structural basis of RIP2 activation and signaling. *Nat Commun.* 2018;9(1):4993.
62. Ellwanger K, Briese S, Arnold C, Kienes I, Heim V, Nachbur U, et al. XIAP controls RIPK2 signaling by preventing its deposition in speck-like structures. *Life Sci Alliance.* 2019;2(4).
63. Solcia E, Sommi P, Necchi V, Vitali A, Manca R, and Ricci V. Particle-rich cytoplasmic structure (PaCS): identification, natural history, role in cell biology and pathology. *Biomolecules.* 2014;4(3):848-61.
64. Maekawa S, Ohto U, Shibata T, Miyake K, and Shimizu T. Crystal structure of NOD2 and its implications in human disease. *Nat Commun.* 2016;7:11813.
65. Adler J, Rangwalla SC, Dwamena BA, and Higgins PD. The prognostic power of the NOD2 genotype for complicated Crohn's disease: a meta-analysis. *Am J Gastroenterol.* 2011;106(4):699-712.
66. Boyle JP, Mayle S, Parkhouse R, and Monie TP. Comparative Genomic and Sequence Analysis Provides Insight into the Molecular Functionality of NOD1 and NOD2. *Front Immunol.* 2013;4:317.
67. Vijayrajratnam S, Pushkaran AC, Balakrishnan A, Vasudevan AK, Biswas R, and Mohan CG. Understanding the molecular differential recognition of muramyl peptide ligands by LRR domains of human NOD receptors. *Biochem J.* 2017;474(16):2691-711.
68. Zhou H, Coveney AP, Wu M, Huang J, Blankson S, Zhao H, et al. Activation of Both TLR and NOD Signaling Confers Host Innate Immunity-Mediated Protection Against Microbial Infection. *Front Immunol.* 2018;9:3082.
69. Boyle JP, Parkhouse R, and Monie TP. Insights into the molecular basis of the NOD2 signalling pathway. *Open Biol.* 2014;4(12).

70. Ghosh P, Rangamani P, and Kufareva I. The GAPs, GEFs, GDIs and…now, GEMs: New kids on the heterotrimeric G protein signaling block. *Cell Cycle.* 2017;16(7):607-12.
71. Getz M, Swanson L, Sahoo D, Ghosh P, and Rangamani P. A predictive computational model reveals that GIV/girdin serves as a tunable valve for EGFR-stimulated cyclic AMP signals. *Mol Biol Cell.* 2019;30(13):1621-33.
72. Kim D, Kim YG, Seo SU, Kim DJ, Kamada N, Prescott D, et al. Nod2-mediated recognition of the microbiota is critical for mucosal adjuvant activity of cholera toxin. *Nat Med.* 2016;22(5):524-30.
73. Heerasing N, and Kennedy NA. Interaction Between NOD2 and Smoking in the Pathogenesis of Crohn's Disease. *EBioMedicine.* 2017;21:49-50.
74. Lécine P, Esmiol S, Métais JY, Nicoletti C, Nourry C, McDonald C, et al. The NOD2-RICK complex signals from the plasma membrane. *J Biol Chem.* 2007;282(20):15197-207.
75. McDonald C, Chen FF, Ollendorff V, Ogura Y, Marchetto S, Lécine P, et al. A role for Erbin in the regulation of Nod2-dependent NF-kappaB signaling. *J Biol Chem.* 2005;280(48):40301-9.
76. Pizarro TT, Pastorelli L, Bamias G, Garg RR, Reuter BK, Mercado JR, et al. SAMP1/YitFc mouse strain: a spontaneous model of Crohn's disease-like ileitis. *Inflamm Bowel Dis.* 2011;17(12):2566-84.
77. Sahoo D, Dill DL, Tibshirani R, and Plevritis SK. Extracting binary signals from microarray time-course data. *Nucleic Acids Res.* 2007;35(11):3705-12.
78. Kanehisa M, and Goto S. KEGG: kyoto encyclopedia of genes and genomes. *Nucleic Acids Res.* 2000;28(1):27-30.
79. Monaco G, Lee B, Xu W, Mustafah S, Hwang YY, Carré C, et al. RNA-Seq Signatures Normalized by mRNA Abundance Allow Absolute Deconvolution of Human Immune Cell Types. *Cell Rep.* 2019;26(6):1627-40.e7.
80. Pavlou S, Wang L, Xu H, and Chen M. Higher phagocytic activity of thioglycollate-elicited peritoneal macrophages is related to metabolic status of the cells. *J Inflamm (Lond).* 2017;14:4.
81. Das S, Owen KA, Ly KT, Park D, Black SG, Wilson JM, et al. Brain angiogenesis inhibitor 1 (BAI1) is a pattern recognition receptor that mediates macrophage binding and engulfment of Gram-negative bacteria. *Proc Natl Acad Sci U S A.* 2011;108(5):2136-41.
82. Sarkar A, Tindle C, Pranadinata RF, Reed S, Eckmann L, Stappenbeck TS, et al. ELMO1 Regulates Autophagy Induction and Bacterial Clearance During Enteric Infection. *J Infect Dis.* 2017;216(12):1655-66.
83. Sayed IM, Suarez K, Lim E, Singh S, Pereira M, Ibeawuchi SR, et al. Host engulfment pathway controls inflammation in inflammatory bowel disease. *Febs j.* 2020;287(18):3967-88.
84. Asai M, Asai N, Murata A, Yokota H, Ohmori K, Mii S, et al. Similar phenotypes of Girdin germ-line and conditional knockout mice indicate a crucial role for Girdin in the nestin lineage. *Biochem Biophys Res Commun.* 2012;426(4):533-8.
85. Thompson LR, Sanders JG, McDonald D, Amir A, Ladau J, Locey KJ, et al. A communal catalogue reveals Earth's multiscale microbial diversity. *Nature.* 2017;551(7681):457-63.
86. de Muinck EJ, Trosvik P, Gilfillan GD, Hov JR, and Sundaram AYM. A novel ultra high-throughput 16S rRNA gene amplicon sequencing library preparation method for the Illumina HiSeq platform. *Microbiome.* 2017;5(1):68.
87. Walters W, Hyde ER, Berg-Lyons D, Ackermann G, Humphrey G, Parada A, et al. Improved Bacterial 16S rRNA Gene (V4 and V4-5) and Fungal Internal Transcribed Spacer Marker Gene Primers for Microbial Community Surveys. *mSystems.* 2016;1(1).
88. Marotz C, Sharma A, Humphrey G, Gottel N, Daum C, Gilbert JA, et al. Triplicate PCR reactions for 16S rRNA gene amplicon sequencing are unnecessary. *Biotechniques.* 2019;67(1):29-32.
89. Bolyen E, Rideout JR, Dillon MR, Bokulich NA, Abnet CC, Al-Ghalith GA, et al. Reproducible, interactive, scalable and extensible microbiome data science using QIIME 2. *Nat Biotechnol.* 2019;37(8):852-7.
90. Callahan BJ, McMurdie PJ, Rosen MJ, Han AW, Johnson AJ, and Holmes SP. DADA2: High-resolution sample inference from Illumina amplicon data. *Nat Methods.* 2016;13(7):581-3.
91. Lahti L, and Shetty S. Tools for microbiome analysis in R. Version http://microbiome.github.com/microbiome.
92. Bhinder G, Sham HP, Chan JM, Morampudi V, Jacobson K, and Vallance BA. The Citrobacter rodentium mouse model: studying pathogen and host contributions to infectious colitis. *J Vis Exp.* 2013(72):e50222.

93. Koroleva EP, Halperin S, Gubernatorova EO, Macho-Fernandez E, Spencer CM, and Tumanov AV. Citrobacter rodentium-induced colitis: A robust model to study mucosal immune responses in the gut. *J Immunol Methods.* 2015;421:61-72.
94. Chassaing B, Aitken JD, Malleshappa M, and Vijay-Kumar M. Dextran sulfate sodium (DSS)-induced colitis in mice. *Curr Protoc Immunol.* 2014;104:Unit 15 25.
95. Kiesler P, Fuss IJ, and Strober W. Experimental Models of Inflammatory Bowel Diseases. *Cell Mol Gastroenterol Hepatol.* 2015;1(2):154-70.
96. Kim JJ, Shajib MS, Manocha MM, and Khan WI. Investigating intestinal inflammation in DSS-induced model of IBD. *J Vis Exp.* 2012(60).
97. Travassos LH, Carneiro LA, Ramjeet M, Hussey S, Kim YG, Magalhães JG, et al. Nod1 and Nod2 direct autophagy by recruiting ATG16L1 to the plasma membrane at the site of bacterial entry. *Nat Immunol.* 2010;11(1):55-62.
98. Linderson Y, Bresso F, Buentke E, Pettersson S, and D'Amato M. Functional interaction of CARD15/NOD2 and Crohn's disease-associated TNFalpha polymorphisms. *Int J Colorectal Dis.* 2005;20(4):305-11.
99. Sabbah A, Chang TH, Harnack R, Frohlich V, Tominaga K, Dube PH, et al. Activation of innate immune antiviral responses by Nod2. *Nat Immunol.* 2009;10(10):1073-80.
100. Ghosh P, Garcia-Marcos M, Bornheimer SJ, and Farquhar MG. Activation of Galphai3 triggers cell migration via regulation of GIV. *J Cell Biol.* 2008;182(2):381-93.
101. Ghosh P, Beas AO, Bornheimer SJ, Garcia-Marcos M, Forry EP, Johannson C, et al. A G{alpha}i-GIV molecular complex binds epidermal growth factor receptor and determines whether cells migrate or proliferate. *Mol Biol Cell.* 2010;21(13):2338-54.
102. Dyer BW, Ferrer FA, Klinedinst DK, and Rodriguez R. A noncommercial dual luciferase enzyme assay system for reporter gene analysis. *Anal Biochem.* 2000;282(1):158-61.
103. Newman JV, Zabel BA, Jha SS, and Schauer DB. Citrobacter rodentium espB is necessary for signal transduction and for infection of laboratory mice. *Infect Immun.* 1999;67(11):6019-25.
104. Bouladoux N, Harrison OJ, and Belkaid Y. The Mouse Model of Infection with Citrobacter rodentium. *Curr Protoc Immunol.* 2017;119:19.5.1-.5.25.
105. Schauer DB, and Falkow S. Attaching and effacing locus of a Citrobacter freundii biotype that causes transmissible murine colonic hyperplasia. *Infect Immun.* 1993;61(6):2486-92.
106. Holgersen EM, Gandhi S, Zhou Y, Kim J, Vaz B, Bogojeski J, et al. Transcriptome-Wide Off-Target Effects of Steric-Blocking Oligonucleotides. *Nucleic Acid Ther.* 2021;31(6):392-403.
107. Garcia-Marcos M, Ghosh P, and Farquhar MG. GIV is a nonreceptor GEF for G alpha i with a unique motif that regulates Akt signaling. *Proc Natl Acad Sci U S A.* 2009;106(9):3178-83.
108. Bhandari D, Lopez-Sanchez I, To A, Lo IC, Aznar N, Leyme A, et al. Cyclin-dependent kinase 5 activates guanine nucleotide exchange factor GIV/Girdin to orchestrate migration-proliferation dichotomy. *Proc Natl Acad Sci U S A.* 2015;112(35):E4874-83.